Surface reflectance of Mars observed by CRISM/MRO:
1. Multi-angle Approach for Retrieval of Surface Reflectance from CRISM observations (MARS-ReCO)

X. Ceamanos,[1,2] S. Douté,[1] J. Fernando,[3,4] F. Schmidt,[3,4] P. Pinet,[5,6] and A. Lyapustin[7]

[1] This article addresses the correction for aerosol effects in near-simultaneous multi-angle observations acquired by the Compact Reconnaissance Imaging Spectrometer for Mars (CRISM) aboard the Mars Reconnaissance Orbiter. In the targeted mode, CRISM senses the surface of Mars using 11 viewing angles, which allow it to provide unique information on the scattering properties of surface materials. In order to retrieve these data, however, appropriate strategies must be used to compensate the signal sensed by CRISM for aerosol contribution. This correction is particularly challenging as the photometric curve of these suspended particles is often correlated with the also anisotropic photometric curve of materials at the surface. This article puts forward an innovative radiative transfer-based method named Multi-angle Approach for Retrieval of Surface Reflectance from CRISM Observations (MARS-ReCO). The proposed method retrieves photometric curves of surface materials in reflectance units after removing aerosol contribution. MARS-ReCO represents a substantial improvement regarding previous techniques as it takes into consideration the anisotropy of the surface, thus providing more realistic surface products. Furthermore, MARS-ReCO is fast and provides error bars on the retrieved surface reflectance. The validity and accuracy of MARS-ReCO is explored in a sensitivity analysis based on realistic synthetic data. According to experiments, MARS-ReCO provides accurate results (up to 10% reflectance error) under favorable acquisition conditions. In the companion article, photometric properties of Martian materials are retrieved using MARS-ReCO and validated using in situ measurements acquired during the Mars Exploration Rovers mission.

Citation: Ceamanos, X., S. Douté, J. Fernando, F. Schmidt, P. Pinet, and A. Lyapustin (2013), Surface reflectance of Mars observed by CRISM/MRO: 1. Multi-angle Approach for Retrieval of Surface Reflectance from CRISM observations (MARS-ReCO), *J. Geophys. Res. Planets*, *118*, doi:10.1029/2012JE004195.

1. Introduction

[2] Imaging spectroscopy is a key remote sensing technique to study the composition, the mineralogy, and the physical state of planetary surfaces. A new generation of imaging spectrometers has recently emerged in the field of space exploration by incorporating an angular dimension of measurement. Multi-angle imaging spectroscopy is conceived to provide a more accurate characterization of planetary materials from

orbit and a higher success in separating the signals coming from the atmosphere and the surface [*Martonchik et al.*, 2009]. The Compact Reconnaissance Imaging Spectrometer for Mars (CRISM) aboard the Mars Reconnaissance Orbiter (MRO) is a visible/short-wave infrared hyperspectral camera that can operate systematically in multi-angle mode from space [*Murchie et al.*, 2007]. In the targeted mode, CRISM measures radiative energy coming from the planet Mars within 0.36–3.92 microns using 544 spectral bands. As shown in Figure 1, CRISM targeted observations are composed of a quasi-nadir hyperspectral image at a spatial resolution of up to 18 m/pixel accompanied by ten $10\times$ spatially binned hyperspectral images which are captured before and after the central scan. This sequence of off-nadir scans called emission phase function (EPF) encompasses view zenith angles up to 70° and two modes of relative azimuth, corresponding to the inbound and outbound portions of the satellite flyby. CRISM targeted observations can sense a given Martian site using different atmospheric paths and thus have proved to be of great value in atmospheric studies [*Smith et al.*, 2009; *Wolff et al.*, 2009]. In addition, this multi-angle data may be exploited to separate atmospheric and surface contributions when analyzed

[1]Université Joseph Fourier/CNRS, Institut de Planétologie et d'Astrophysique de Grenoble (IPAG), UMR 5274, Grenoble, France.
[2]Météo-France/CNRS, CNRM/GAME, Toulouse, France.
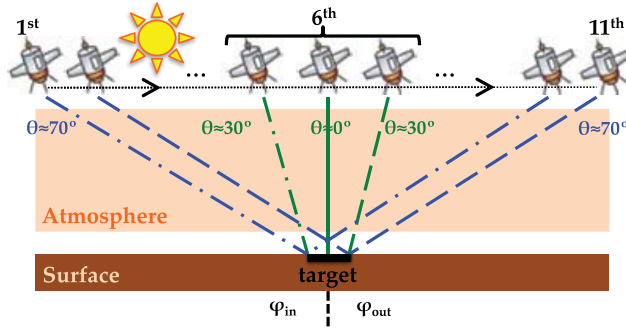[3]Université Paris-Sud, Laboratoire IDES, UMR 8148, Orsay, France.
[4]CNRS, Orsay, France.
[5]Université de Toulouse, UPS-OMP, IRAP, Toulouse, France.
[6]CNRS, IRAP, Toulouse, France.
[7]NASA GSFC, Greenbelt, Maryland, USA.

Corresponding author: X. Ceamanos, GAME, CNRM, Météo-France, CNRS, 42 avenue Gaspard Coriolis, 31057 Toulouse, France. (xavier.ceamanos@meteo.fr)

Figure 1. Schema of a CRISM targeted observation. Only three images out of 11 are shown. The central scan at full spatial resolution is drawn in green, while the most extreme scans of the EPF are pictured in blue. Dash-dotted and dashed lines depict the first and last scanned lines of each single image, respectively. All scans are acquired as a combination of the gimbal and the motion of MRO which results in a VZA range of $\theta \in [0°, 30°]$ for the quasi-nadir central scan. The two modes in relative azimuth ($\varphi_{in} + \varphi_{out} \approx 180°$) are shown.

using a radiative transfer model accounting for surface scattering and atmospheric extinction [*Murchie et al.*, 2007]. The combination of an adequate atmospheric correction and the multi-angle capabilities of CRISM may make possible the retrieval of photometric properties of the surface according to observation geometry and wavelength. These surface products are essential to characterize the physical state of Martian materials as well as to distinguish between different types of terrains [*Johnson et al.*, 2006a, 2006b; *Jehl et al.*, 2008].

[3] The atmosphere of Mars is quite thin and mainly composed of carbon dioxide (CO_2) gas and suspended mineral and water ice particles named aerosols [*Barlow*, 2008]. These components represent an obstacle to remotely sensing the Martian surface as extinction of solar irradiance in the visible/short-wave infrared range happens by gaseous absorption and aerosol scattering and absorption. The modeling of the radiation reaching the top-of-atmosphere (TOA) level therefore demands an adequate characterization of both components [*Clancy and Lee*, 1991; *Drossart et al.*, 1991; *Erard et al.*, 1994; *Ockert-Bell et al.*, 1997; *Tomasko et al.*, 1999; *Korablev et al.*, 2005; *Wolff et al.*, 2009]. Atmospheric correction algorithms compensate the sensed TOA radiances for atmospheric contribution through the inversion of such atmosphere/surface models in order to retrieve surface quantities. One of the main hurdles to achieve an accurate correction is that aerosols and materials at the surface scatter light anisotropically depending on illumination and viewing conditions and are rarely spectrally distinct. Retrieval of accurate estimates of surface reflectance therefore requires the consideration, in the radiative transfer model, of the scattering phase function of aerosols as well as the bidirectional reflectance distribution function (BRDF) of the surface. In this context, the availability of multiple TOA measurements with different angular configurations, together with the implementation of appropriate techniques, becomes necessary to solve as accurately as possible the inverse problem [*Martonchik*, 1994]. In practice, atmospheric correction strategies are devised to retrieve the surface BRDF assuming an aerosol phase function.

[4] While correction for atmospheric gases is generally possible for non-icy surfaces [*Langevin et al.*, 2005; *McGuire et al.*, 2009], compensation for aerosol contribution represents a major challenge. Aerosol content on Mars is very variable as these particles are highly mobilized during storms which range from local events to global storms covering the entire planet. The variability of aerosol content in time and space is generally overcome by estimating, for each spacecraft orbital path, the local atmospheric opacity or the aerosol optical depth (AOD). For instance, *Vincendon et al.* [2007] propose to retrieve surface reflectance from observations taken by the hyperspectral imager "Observatoire pour la Minéralogie, l'Eau, les Glaces, et l'Activité" (OMEGA) aboard the Mars Express orbiter after quantifying the contribution of atmospheric aerosols using a Monte Carlo method. In that study, the need of multi-angle data is satisfied by processing several nadir observations acquired over the same target at different times, resulting in different solar zenith angles, and assuming that the AOD remains constant along the time span (up to several days). Besides this supposition, the surface is assumed to be characterized by a wavelength-dependent angular-independent single reflectance value called Lambertian albedo. The Lambertian assumption supposes that variations of TOA radiance with geometry are exclusively related to aerosols. This hypothesis is also adopted by *McGuire et al.* [2008] to process the central scan of CRISM targeted observations by a radiative transfer approach that computes surface spectra in Lambertian albedo units after correction for gaseous and aerosol contributions. Alternatively, *Brown and Wolff* [2009] propose to exploit the multi-angle information enclosed in CRISM targeted observations by modeling the remotely sensed signal at a single wavelength. Three parameters (surface Lambertian albedo, mineral aerosol opacity, and water ice aerosol opacity) are iteratively adjusted to fit the multi-angle CRISM data. Similarly, a Lambertian surface is also considered by the radiative transfer-based procedure developed by *Wiseman et al.* [2012] to retrieve atmospherically corrected CRISM surface spectra.

[5] In planetary remote sensing, the Lambertian assumption is generally adopted by atmospheric correction techniques, even when multi-angle measurements are available. This supposition substantially simplifies the radiative transfer modeling and reduces the size of the look-up table used in the inversion. The Lambertian hypothesis seems intuitively appropriate in some cases (e.g., turbid atmosphere). However, it has been proved that non-Lambertian, or anisotropic, scattering properties play a significant role for most mineral and icy surfaces [*de Grenier and Pinet*, 1995; *Pinet and Rosemberg*, 2001; *Johnson et al.*, 2006a, 2006b; *Lyapustin et al.*, 2010]. As a consequence, the adoption of a Lambertian assumption can create significant angle-dependent biases in derived surface reflectances [*Lyapustin*, 1999]. To our knowledge, *Cull et al.* [2010] are pioneers in performing surface retrievals from CRISM targeted observations considering a non-Lambertian surface. In that work, the inversion for the surface properties is achieved using a Hapke's model for the surface BRDF and a radiative transfer-simulated look-up table that stores TOA spectra corresponding to multiple atmospheric situations. Nevertheless, the algorithm of *Cull et al.* [2010] is restricted to a few CRISM targeted observations as it assumes that the sensed surface has similar

photometric properties than the materials characterized by the Mars Exploration Rovers (MER) mission at the Gusev crater of Mars.

[6] In the field of Earth remote sensing, some efforts have been done towards the mitigation or the elimination of the Lambertian assumption. *Guanter et al.* [2005] address the atmospheric correction of multi-angle observations acquired by the Compact High Resolution Imaging Spectrometer (CHRIS) aboard the PRoject for On-Board Autonomy (PROBA) under a Lambertian constraint with relaxation. An iterative strategy for surface retrieval is defined by assuming a Lambertian surface on the first iteration and injecting the inferred BRDF into the radiative transfer-based inversion on subsequent iterations until convergence is reached. Although this method improves the quality of the finally estimated BRDF, it may become problematic for highly anisotropic surfaces for which the initial assumption may greatly impact the succeeding retrievals. The incorporation of the BRDF into the atmospheric correction of remotely sensed data is also considered for processing multi-temporal data collected by the MODerate resolution Imaging Spectroradiometer (MODIS) aboard the Terra and Aqua spacecrafts [*Schaaf et al.*, 2002] and the Multi-angle Imaging SpectroRadiometer (MISR) aboard the Terra spacecraft [*Diner et al.*, 2005]. Recently, surface retrievals are carried out for series of multi-temporal images acquired by MODIS by the Multi-angle Implementation of Atmospheric Correction (MAIAC) algorithm *Lyapustin et al.* [2011a, 2011b, 2012]. Contrary to the previous methods, MAIAC solves the aerosol/surface coupling problem without strong reductionist assumptions using an innovative radiative transfer-based formulation of the TOA radiance. The mathematical properties of this formulation combined with the consideration of an advantageous surface BRDF model enable a fast and efficient inversion for the surface reflectance.

[7] To our knowledge, a method to compensate CRISM targeted observations for aerosol contribution considering an unknown non-Lambertian surface is not available in the literature. This article puts forward such a method through an innovative radiative transfer-based strategy that inherits some basis from the MAIAC algorithm. The method under the name of Multi-angle Approach for Retrieval of Surface Reflectance from CRISM Observations (hereafter referred to as MARS-ReCO) is proposed to retrieve surface reflectance from CRISM targeted observations. The major innovation is the consideration of an anisotropic surface, thanks to an accurate quasi-linear parametrization of the TOA radiance. In addition, the algorithm is endowed with a formalism integrating several sources of uncertainty into the inversion process and propagating them to the solution. MARS-ReCO transforms a CRISM targeted observation, originally in units of TOA radiance, into a set of photometric curves with error bars in units of surface reflectance depending on acquisition geometry. MARS-ReCO addresses the correction for mineral aerosols exclusively, thus not dealing with water ice aerosols nor atmospheric gases. The mineral aerosol particle size distribution and refractive index, as well as the AOD of each observation, must be provided beforehand.

[8] The article is organized as follows. The MARS-ReCO approach is detailed in Section 2 as well as the preprocessing of CRISM targeted observations. Section 3 describes the tests conducted to evaluate the performance of MARS-ReCO on CRISM-like synthetic data. Eventually, Section 4 discusses the benefits and limitations of the proposed approach. The capabilities of MARS-ReCO are tested on real CRISM data and validated against MER in situ measurements in the companion article [*Fernando et al.*, 2013]. Note that the present work as well as the companion article restricts the use of MARS-ReCO to spectral bands without gaseous absorption.

2. Methods

[9] MARS-ReCO compensates CRISM targeted observations for mineral aerosol effects. The proposed method inherits the basis from the method named MAIAC [*Lyapustin et al.*, 2012] while adding some functionalities. Contrary to MAIAC, which works with multi-temporal series of images, MARS-ReCO is devised to process near-simultaneous multi-angle CRISM observations. Furthermore, MARS-ReCO takes care of propagating several sources of errors to the end products. Before applying MARS-ReCO, CRISM targeted observations are transformed into appropriate products for multi-angular data processing.

2.1. Preliminaries

2.1.1. Integrated Multi-angle Product

[10] The 11 hyperspectral images forming a CRISM targeted observation are released individually in units of I/F, the ratio of measured intensity to solar flux. Note that the dependency on wavelength of all radiometric quantities in this article is omitted for simplicity. In order to facilitate the simultaneous processing of the multi-angle information associated to each terrain unit, the spectra corresponding to the 10 scans are rearranged in a common geographical grid of super-pixels (i.e., terrain units sensed at more than one geometry) to create a single data set named SPC cube (for SpectroPhotometric Curve). This is done after degrading the spatial resolution of the central scan in coherence with the properties of the EPF. SPC cubes are multi-angle integrated products which facilitate the access to photometric curves. A photometric curve is a series of radiometric measurements at a given wavelength acquired from a specific super-pixel with different angular configurations. The stacking of several photometric curves corresponding to consecutive wavelengths forms a spectrophotometric set. Figure 2 (left) illustrates the typical degree of overlapping by projecting the footprints of the 11 hyperspectral images onto the common geographical space. Note that the overlap is non-optimal, as typically only ~30% of all super-pixels are sensed by four or more angular measurements. Figure 2(center) shows the regular grid that is defined over the resulting mosaic such that each element (i.e., a super-pixel) corresponds to a single terrain unit typically measuring ~450×450 m^2. This value takes into account the decrease in spatial resolution at the edges of the central and EPF images. Under this configuration, each band of a SPC cube contains about 2300 photometric curves, many of them made of less than four measurements. Note that a higher spatial resolution can be achieved only by tossing out the largest EPF super-pixels. Figure 2(right) details the structure of a SPC cube in which each spectrum of a targeted observation is arranged according to its angular configuration (up to 11) along the x axis and according to its spatial location, or super-pixel, along the y axis. For simplicity, super-pixels are arranged according to the number of available
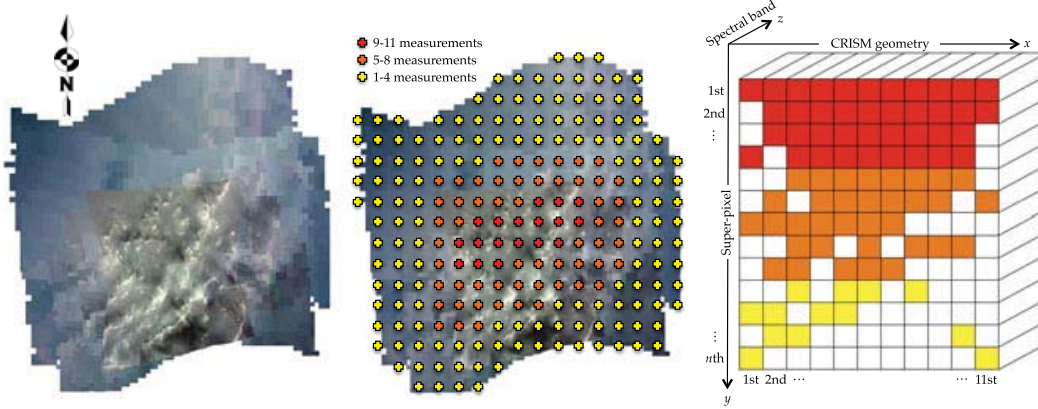
Figure 2. (left) Footprints of the 11 scans of a CRISM observation in a common geographical space. Note the different extent and shape of each image. In this example, the spatial resolution of the central scan has not been degraded for clarity. (center) Schema of the approximative overlaying grid of super-pixels. Each cross indicates the center of the associated super-pixel, while its color is coded according to the number of available angular measurements. (right) Schema of a SPC cube. Each row stores the information belonging to a same super-pixel. Photometric curves follow the same color code that in Figure 2 (center). Blank positions mean absence of angular measurement.

measurements. Under this configuration, each row at a specific spectral band contains a photometric curve while a x-z plane includes a spectrophotometric set, both products being in I/F units. Note that MARS-ReCO processes one spectral band at a time.

2.1.2. Retrieval of Aerosol Content

[11] MARS-ReCO must be fed with an estimate of the AOD associated to the CRISM observation to be processed. In the literature, many authors address this issue with a direct application to CRISM data [*Lemmon et al.*, 2004; *Wolff et al.*, 2009; *Douté and Ceamanos*, 2010]. Note that the performance of MARS-ReCO is sensitive to the accuracy of the AOD estimate. Furthermore, methods avoiding or minimizing the Lambertian surface assumption should be prioritized for consistency with MARS-ReCO.

2.2. Description of the MARS-ReCO Approach

[12] MARS-ReCO is conceived to infer photometric curves of the Martian surface from CRISM multi-angle orbital imagery. The contribution of mineral aerosols to the remotely sensed signal is compensated based on a radiative transfer-based algorithm which is fed by the scattering properties of these atmospheric particles. After fitting a model of the TOA signal to the CRISM measurements, the surface bidirectional reflectance associated to each super-pixel in a SPC cube is retrieved at the acquisition geometries. The theoretical background and the technical aspects of the proposed approach are detailed in the following. The notation used in this article is listed at the end of this document.

[13] The MARS-ReCO algorithm is based on a coupled surface-atmosphere radiative transfer formulation of the TOA signal originally proposed by *Lyapustin and Knyazikhin* [2001] and adapted by *Lyapustin et al.* [2011a] for the MAIAC algorithm. The major keystone of this accurate semi-analytical formulation is the consideration in the radiative transfer equation of a Green's function to model the intrinsic diffuse scattering responses of the atmosphere and a kernel-based scattering model for the surface.

2.2.1. Green's Function of the Atmosphere

[14] Many codes solving the radiative transfer of solar light in the surface-atmosphere interface are not suitable for simulating large collections of spectra because of their large computational requirements. The condition for the lower limit of the radiative transfer (i.e., the surface reflectance) is usually part of the calculation which must be performed for each combination of physical parameters related to the surface and the atmosphere. The Green's function method allows us to circumvent these drawbacks by a partial decoupling of the surface and the atmosphere. *Lyapustin and Knyazikhin* [2001] proved that this method makes possible the analytical combination of the atmospheric reflectivity and transmissivity with the surface reflectance to calculate TOA radiances for an arbitrary aerosol optical depth and acquisition geometry. This is achieved at the price of a small degradation of accuracy coming from two simplifications. Details on the use of a Green's function in the radiative transfer equation and the related assumptions can be found in Appendix A.

2.2.2. Expression for the TOA Reflectance

[15] The radiance reaching the CRISM instrument (L) can be decomposed as a sum of the atmospheric path radiance (D), and the radiance reflected by the surface before being directly (L_s) and diffusely (L_s^d) transmitted through the atmosphere,

$$L(s_0, s) = D(s_0, s) + L_s(s_0, s)e^{-\tau_0/|\mu|} + L_s^d(s_0, s), \quad (1)$$

where s_0 and s are the incidence and view directions. The first term of the surface-reflected radiance can be written as

$$L_s(s_0, s) \cong S\mu_0 e^{-\tau_0/\mu_0}\{\rho(s_0, s) + \alpha c_0 \rho_1(\mu)\rho_2(\mu_0)\} \quad (2)$$

$$+ \frac{\alpha}{\pi}\int_{\Omega^+} D_s\left(s_0, s'\right)\rho\left(s', s\right)\mu' ds',$$

where πS is the extraterrestrial solar spectral irradiance, ρ is the bidirectional reflectance factor (BRF) ($\rho = \pi f$, where f is the BRDF as defined by *Nicodemus et al.* [1977]), c_0 is the spherical albedo of the atmosphere, D_s is the path radiance

incident on the surface, and ρ_1 and ρ_2 are BRF-derived functions described in Appendix A. Parameter α is a multiple reflection factor that depends on the surface albedo $q(\mu_0)$ such that $\alpha = (1 - q(\mu_0)c_0)^{-1}$.

[16] The diffusely transmitted surface-reflected radiance at the TOA can be calculated from L_s with the help of the one-dimensional diffuse Green's function of the atmosphere (G^d) as it is demonstrated in Appendix A,

$$L_s^d(s_0, s) = \int_{\Omega^-} G^d(s_1, s) L_s(s_0, , s_1) ds_1. \tag{3}$$

[17] The quantity πG_d is also called bidirectional upward diffuse transmittance of the atmosphere. The surface albedo is defined as a ratio of reflected and incident radiative fluxes at the surface,

$$q(\mu_0) = F^{Up}(\mu_0)/F^{Down}(\mu_0),$$
$$F^{Down}(\mu_0) = F_s(\mu_0) + F_s^d(\mu_0) = \pi S \mu_0 e^{-\frac{\tau_0}{\mu_0}} + \int_{\Omega^+} D_s\left(s_0, s'\right)\mu' ds',$$
$$F^{Up}(\mu_0) = \pi S \mu_0 e^{-\frac{\tau_0}{\mu_0}} q_2(\mu_0) + \int_{\Omega^+} \mu' q_2\left(\mu'\right) D_s\left(s_0, s'\right) ds',$$
$$q_2(\mu_0) = \frac{1}{\pi} \int_{\Omega^-} \rho(s_0, s)\mu ds.$$
$$\tag{4}$$

[18] These formulas give an explicit expression for the TOA radiance as a function of the surface BRF. Their accuracy is high, usually within a few tenths of a percent [*Lyapustin and Knyazikhin*, 2001]. In the following, we work with units of top-of-atmosphere reflectance which is defined as $R = L/(S\mu_0) = (I/F)/\mu_0$. Note that MARS-ReCO processes SPC cubes which have been previously transformed into units of top-of-atmosphere reflectance. For simplicity, we use the symbol R to refer to units of TOA reflectance in a gas-free atmosphere populated by aerosols.

2.2.3. Surface Scattering Model

[19] The anisotropy of the surface is taken into account through its BRF modeled using a semi-empirical kernel-based Ross-Thick Li-Sparse (RTLS) model [*Lucht et al.*, 2000]. The RTLS model expands the bidirectional reflectance distribution of the surface into a linear sum of terms (the so-called kernels) characterizing different scattering modes. The kernels in the RTLS model are derived from physical theory through simplifying assumptions and approximations. In particular, the surface bidirectional reflectance is decomposed as the sum of (i) a Lambertian—or isotropic—contribution, (ii) a geometric component modeling the diffuse reflection taking into account the 3D geometrical structure of opaque reflectors on the surface and shadowing phenomena, and (iii) a volume scattering contribution simulated by a collection of dispersed facets. In this way the BRF is written as

$$\rho(\mu_0, \mu, \varphi) = k^L + k^G f_G(\mu_0, \mu, \varphi) + k^V f_V(\mu_0, \mu, \varphi), \tag{5}$$

where subscripts refer to Lambertian (L), geometric (G), and volumetric (V) components, and f_G, f_V are predefined geometric kernels. More details on the RTLS kernels can be found in Appendix B.

[20] The RTLS model is very advantageous to shape efficient inversion algorithms based on radiative transfer [*Schaaf et al.*, 2002; *Lyapustin et al.*, 2012] as the surface bidirectional reflectance is characterized by a linear combination of three

invariant kernels scaled by their corresponding kernels weights $\mathbf{k} = \{k^L, k^G, k^V\}$. While they are not perfectly orthogonal functions, they are sufficiently independent to allow stable recovery of the parameters for many angular sampling distributions [*Lucht et al.*, 2000]. Furthermore, the RTLS model has proved to be accurate in recreating many types of natural surface ranging from highly anisotropic snow-covered terrains [*Lyapustin et al.*, 2010] to backscattering surfaces such as those found in vegetation [*Schaaf et al.*, 2002]. In particular, the geometric kernel models the backscattering features at the smallest CRISM phase angles ($g \approx 30°$).

2.2.4. Expression for the TOA Reflectance Using the RTLS Surface Model

[21] The substitution of equation (5) into equations (1)–(4) (after normalization to reflectance units and separation of the kernel weights) provides the following quasi-linear expression for the TOA reflectance:

$$R(\mu_o, \mu, \varphi) = R^D(\mu_o, \mu, \varphi) + k^L F^L(\mu_o, \mu)$$
$$+ k^G F^G(\mu_o, \mu, \varphi) + k^V F^V(\mu_o, \mu, \varphi) + R^{nl}(\mu_o, \mu), \tag{6}$$

where R^D stands for the atmospheric path reflectance coming from photons scattered by aerosols without interacting with the surface. Quantities $\{F^L, F^G, F^V\}$, on the one hand, and R^{nl}, on the other hand, are multiplicative factors for the kernel weights $\mathbf{k}$ and a nonlinear term, respectively,

$$F^L(\mu_o, \mu) = \left(e^{-\tau_0/\mu_0} + \alpha\mu_0^{-1} F_s^d(\mu_0)/(\pi S)\right)\left(e^{-\tau_0/|\mu|} + G^{av}(\mu)\right),$$

$$F^k(\mu_o, \mu, \varphi) = \{e^{-\tau_0/\mu_0} f_k(\mu_0, \mu, \varphi) + \alpha\mu_0^{-1} D_k^1(\mu_0, \mu, \varphi)\} e^{-\tau_0/|\mu|} \tag{7}$$
$$+ e^{-\tau_0/\mu_0} G_k^1(\mu_0, \mu, \varphi) + \alpha\mu_0^{-1} H_k^1(\mu_0, \mu, \varphi), \tag{8}$$

$$R^{nl}(\mu_o, \mu) = \alpha c_0 \rho_2(\mu_o) e^{-\tau_0/\mu_0} \{e^{-\tau_0/|\mu|}\rho_1(\mu) + k^L G^{av}(\mu) \tag{9}$$
$$+ k^G G_G^{11}(\mu) + k^V G_V^{11}(\mu)\},$$

where the subscript k refers to either geometric (G) or volumetric (V) kernels. Quantities D_G^1, D_V^1, G^{av}, G_G^1, G_V^1, G_G^{11}, G_V^{11}, H_G^1, and H_V^1 represent different integrals of the incident path radiance (D_s) and/or the atmospheric Green's function (G^d) with the RTLS kernels (f_G, f_V). The integral expression for these functions can be found in *Lyapustin and Wang* [2005]. Contrary to R^{nl}, which strongly depends on the surface by means of functions ρ_1 and ρ_2, quantities $\{F^L, F^G, F^V\}$ depend only weakly through the multiple reflection factor (α). Equation 6 describes the TOA reflectance as an explicit quasi-linear function of the RTLS kernel weights, thus provides the means for an efficient inversion.

2.2.5. Look-up Table

[22] As it will be explained, the retrieval of the surface kernel weights $\mathbf{k}$ is possible through the inversion of equation (6) subject to the availability of quantities R^D, $\{F^L, F^G, F^V\}$, and R^{nl}. A look-up table is generated to store R^D and all surface-independent radiometric quantities allowing us to calculate $\{F^L, F^G, F^V\}$ and R^{nl}. In particular, the look-up table includes the basic quantities R^D, D_s, c_0, and G^d as well as the intermediate quantities D_G^1, D_V^1, G^{av}, G_G^1, G_V^1, G_G^{11}, G_V^{11}, H_G^1, and H_V^1.

[23] Basic quantities are computed using the radiative transfer program named Discrete Ordinates Radiative Transfer Program for a Multi-layered Plane-Parallel Medium

(DISORT) [*Stamnes et al.*, 1988]. For a homogeneous aerosol layer with opacity τ_0, the atmospheric reflected path reflectance (R^D) is computed considering a dark surface (surface albedo set to 0) and simulating the radiation at the sensor level. The path radiance incident on the surface (D_s) is computed similarly but considering this time the downward radiance at the lower interface. The spherical albedo of the atmosphere (c_0) is obtained after integration of its directional-hemispherical version which is directly provided by DISORT. Eventually, the diffuse Green's function of the atmosphere (G^d) is calculated similarly to D_s but reversing the direction of light propagation. In other words, the atmospheric layers must be set in reverse order and the result must be normalized by πS_λ [*Lyapustin and Knyazikhin*, 2001]. In the case of an homogeneous atmosphere, the problem for the Green's function becomes identical to the problem for D_s provided the substitution $s_0 \rightarrow s$. A completely dark surface is also considered to avoid multiple reflections between the surface and the atmosphere. The calculation of the intermediate quantities from the basic functions and the RTLS kernels is explained in *Lyapustin and Wang* [2005].

[24] A homogeneous atmosphere made of a single layer of mineral aerosols is used to compute the basic quantities look-up table. Besides its simplicity, this atmospheric model is appropriate to compute a "universal" look-up table representing the average Martian atmosphere. This model supposes that uncertainties related to mineral aerosols (i.e., AOD estimate, particle size, and refractive indexes) are negligible and that water clouds are not present. If the latter particles become significant, a stratified atmosphere should be considered. However, the correction for atmospheric water ice is out of the scope of this work. The radiative properties of the mineral aerosol particles (phase function and single-scattering albedo) are taken from the work of *Wolff et al.* [2009] in which Martian aerosols are modeled as cylindrical particles with an effective radius of 1.5 μm.

[25] All radiometric quantities stored in the look-up table are computed for several values of τ_0 and $\{\mu_0,\mu,\varphi\}$ to encompass different scenarios regarding atmospheric conditions and acquisition geometry, respectively. The angular grid density of the look-up table is selected empirically based on a trade-off between inversion accuracy and required memory. The angular range encompassed by CRISM targeted observations is taken into account by computing the look-up table at $\theta_0 \in [14°, 81°]$, $\theta \in [0°, 70°]$, and $\varphi \in [0°, 180°]$, with $\Delta\mu_0 = \Delta\mu = 0.02$ and $\Delta\varphi = 3°$. A nearest neighbor technique is selected to fit CRISM observations to the pre-computed look-up table. In this way, we avoid a costly interpolation in the angular triplet $\{\mu_0,\mu,\varphi\}$ that should be done for each CRISM angular measurement otherwise. On the other hand, the look-up table is computed for a set of 12 atmospheric opacities values, namely, $\tau_0(1\ \mu m) = \{0,0.05,0.1,0.2,0.33,0.5,0.75,1,1.4,2.0,2.8,4.0\}$. The look-up table is not homogeneously sampled in terms of AOD since the contribution of a changing aerosol content to the remotely sensed signal is more variable for a low AOD. A linear interpolation is used to obtain the look-up table values for a specific AOD. Under this configuration, the size of the look-up table is low (~50 megabytes per spectral band) due to its independence on the surface kernel weights $\mathbf{k}$. Note that the look-up table is computed only once and can be then used for any CRISM observation.

2.2.6. Inversion Strategy for Surface Reflectance

[26] MARS-ReCO retrieves the photometric curve in BRF units corresponding to each super-pixel of a SPC cube by inverting the TOA reflectance model in equation (6). This is done based on the look-up table described above. An iterative inversion strategy is proposed based on a formalism borrowed from *Tarantola* [2005], which integrates several sources of uncertainty in the inversion process and propagates them to the solution.

2.2.6.1. Basis and Objective of the Inversion

[27] Let $\mathbf{R}^C = \left\{ R^C_1, \ldots, R^C_{Ng} \right\}$ be the photometric curve in units of TOA reflectance measured by CRISM at a given gas-free spectral band. The term Ng is the number of available angular measurements, where $Ng \leq 11$ in the case of CRISM targeted observations. Let $\mathbf{R}^C$ be associated to a given super-pixel of the SPC cube which corresponds to a portion of Martian surface characterized by the state vector $\mathbf{k} = \{k^L, k^G, k^V\}$, whose elements are unknown at first. Let $\mathbf{k}_{sol}$ be the RTLS kernel weights that provide the best fit between the observed data $\mathbf{R}^C$ and the predicted photometric curve $\mathbf{R} = \{R_1, \ldots, R_{Ng}\}$, which is built using equation (6). The comparison is done by means of the root mean square error (RMSE) as follows:

$$RMSE = \sqrt{\frac{1}{N_g} \sum_{j=1}^{N_g} \left(R^C_j - R_j \right)^2}. \quad (10)$$

[28] The solution $\mathbf{k}_{sol}$ is therefore the set of kernel weights that minimizes the RMSE such that $\mathbf{k}_{sol} = \arg\min_{\mathbf{k}} RMSE$. MARS-ReCO addresses the obtention of the triplet $\mathbf{k}_{sol}$ for every photometric curve in a CRISM targeted observation. This triplet allows us to compute the surface BRF at the N_g sampled geometries by means of the RTLS model (equation (5)). Also, the existing uncertainties are taken into account and propagated to put error bars to the retrieved solution $\mathbf{k}_{sol}$ and the associated surface reflectance values.

2.2.6.2. Composition of the Inversion Matrix and Assumptions on the First Iteration

[29] The model relating the state vector $\mathbf{k}$ to the TOA reflectances $\mathbf{R}$ (i.e., equation (6)) is initially dependent on the surface properties due to the nonlinear term R^{nl} and, to a lesser extent, the quantities $\{F^L, F^G, F^V\}$. As a solution, we follow *Lyapustin et al.* [2012] who propose to retrieve $\mathbf{k}_{sol}$ through an iterative inversion algorithm. Let $\mathbf{r}^{(0)} = \left\{ r^{(0)}_1, \ldots r^{(0)}_{Ng} \right\}$ be a set of reduced measurements on the first iteration $n = 0$ where $r^{(0)}_j = R_j - R^D_j - R^{nl(0)}_j$. Using equation (6) and a matrix form, we read

$$\mathbf{r}^{(0)} = \mathbf{F}^{(0)}\mathbf{k}, \qquad \mathbf{F}^{(0)} = \begin{bmatrix} F^{L(0)}_1 & F^{G(0)}_1 & F^{V(0)}_1 \\ \vdots & \vdots & \\ F^{L(0)}_j & F^{G(0)}_j & F^{V(0)}_j \\ \vdots & \vdots & \\ F^{L(0)}_{N_g} & F^{G(0)}_{N_g} & F^{V(0)}_{N_g} \end{bmatrix}. \quad (11)$$

[30] *Lyapustin et al.* [2012] remove the dependence on the surface by assuming a black surface on the first iteration, that is, $\mathbf{k}^{(0)} = \{0,0,0\}$. This supposition, however, results in longer convergence times for bright surfaces such as those found on the high latitudes of Mars. As a consequence, MARS-ReCO

assumes an isotropic surface on the first iteration $\mathbf{k}^{(0)} = \{R^C_{bck}, 0, 0\}$, where the subscript *bck* corresponds to the CRISM geometry in which aerosols are less predominant, that is, the backscattering direction. This assumption is generally possible because the majority of CRISM targeted observations are split into two modes of relative azimuth (review Figure 1), one of them corresponding to low φ values.

[31] This assumption allows the iterative process to start by computing $\mathbf{F}^{(0)}$ through the evaluation of the look-up table at the angular triplet $\{\mu_{0j}, \mu_j, \varphi_j\}$ of each measurement R^C_j and at the atmospheric input τ_0. We remember that the look-up table is linearly interpolated according to τ_0 and a nearest neighbor method is used in the geometric dimension. Similarly, the quantity $R^D_j(\tau_0) + R^{nl}_j(\mathbf{k}^{(0)}, \tau_0)$ is computed knowing τ_0 and $\mathbf{k}^{(0)}$.

2.2.6.3. Characterizing the Uncertainties

[32] In order to propagate the existing uncertainties, the a posteriori covariance matrix of the state vector $(\mathbf{C}_k)$ is calculated. The state vector $\mathbf{k}$ is considered a random variable. For this purpose, we use the formalism of *Tarantola* [2005] in the framework of (i) a linear model that relates $\mathbf{k}$ to the set of reduced measurements $\mathbf{r}^{(0)}$ and (ii) a set of Gaussian probability distribution functions (PDFs) pertaining to the input and output parameters of the inversion problem. Each PDF expresses different information at different steps of the process (i.e., evaluation of the most probable AOD and its related uncertainty, a priori knowledge on the state of the system, CRISM measurements, and the top-of-atmosphere reflectance model). We note two types of uncertainties on vector $\mathbf{r}^{(0)}$:

1. The error on the CRISM measurements R^C_j, which is assumed to be independent on the state of the system and the other geometries, with a diagonal covariance matrix $\mathbf{C}_C$ with elements $\sigma^2_1, \ldots, \sigma^2_{N_g}$.
2. The error on the AOD estimation τ_0, which induces an error on $R^D_j + R^{nl(0)}_j$. In this case, we also assume the independence regarding the state of the system and the other geometries. We evaluate the elements of the covariance matrix experimentally by generating a random series of values according to a Gaussian PDF with mean τ_0 and variance $\sigma^2_{\tau_0}$. We then calculate, based on the TOA reflectance model in equation (6), the population of samples $R^D_j(\tau_0) + R^{nl}_j(\mathbf{k}^{(0)}, \tau_0)$ for each geometry $j \in [1, N_g]$. Likewise, the covariance matrix $\mathbf{C}^{(0)}_{\tau_0}$ is computed using a classical estimator.

[33] The total covariance matrix for the reduced measurements is $\mathbf{C}^{(0)}_r = \mathbf{C}_C + \mathbf{C}^{(0)}_{\tau_0}$. Last but not least, we have some a priori information on the solution in the form of a PDF characterized by its mean $\mathbf{k}^{(0)}$ and a covariance matrix $\mathbf{C}_k$ that we suppose to be diagonal with elements σ^2_L, σ^2_V, and σ^2_G taking large values.

2.2.6.4. Retrieval of Surface Reflectance and Propagation of Errors

[34] In the framework of the linear model and the Gaussian PDFs, the most likely a posteriori state vector $\mathbf{k}^{(1)}$ and the a posteriori covariance matrices $\mathbf{C}_{kp}$ and $\mathbf{C}_{rp}$—respectively associated to $\mathbf{k}^{(1)}$ and the model of TOA reflectance—are retrieved through the explicit least-squares solution proposed by *Tarantola* [2005]:

$$\mathbf{k}^{(1)} = \mathbf{k}^{(0)}$$
$$+ \mathbf{C}_k \mathbf{F}^{(0)T} \left(\mathbf{F}^{(0)} \mathbf{C}_k \mathbf{F}^{(0)T} + \mathbf{C}^{(0)}_r \right)^{-1} \left(\mathbf{r}^{(0)} - \mathbf{F}^{(0)} \mathbf{k}^{(0)} \right), \quad (12)$$
$$\mathbf{C}_{kp} = \mathbf{C}_k - \mathbf{C}_k \mathbf{F}^{(0)T} \left(\mathbf{F}^{(0)} \mathbf{C}_k \mathbf{F}^{(0)T} + \mathbf{C}^{(0)}_r \right)^{-1} \mathbf{F}^{(0)} \mathbf{C}_k, \quad (13)$$
$$\mathbf{C}_{rp} = \mathbf{F}^{(0)} \mathbf{C}_{kp} \mathbf{F}^{(0)T} + \mathbf{C}^{(0)}_\tau. \quad (14)$$

[35] Vector $\mathbf{k}^{(1)}$ provides a refined estimate of the surface BRF and, consequently, of the model $\mathbf{F}^{(1)}$. These two quantities are used in the upcoming iteration $n = 1$. Furthermore, the reduced measurement vector and its associated covariance matrix are updated through the calculation of $R^{nl(1)}$ to give $\mathbf{r}^{(1)}$ and $\mathbf{C}^{(1)}_r$. This iterative process is repeated for several iterations before stopping on the iteration m after MARS-ReCO decides that the triplet of weights is satisfactory (i.e., $\mathbf{k}^{(m)} \sim \mathbf{k}_{sol}$). As it is explained below, the number of iterations is set automatically according to the goodness of the retrieved surface BRF model.

2.2.6.5. Refinement of Surface Solution by Iterative Method

[36] A convergence criterion is defined to refine the surface solution through several iterations. However, the physical sense of the retrieved BRF is not always assured. Indeed, the retrieved BRF model can be related to an incorrect shape (e.g., negative BRF values at some angles) despite a high goodness of fit at the measurement angles. This situation is likely to happen due to a deficient radiometric quality, a limited angular sampling, or a high aerosol content. For this reason, the quality of the input TOA photometric curve and the output retrieved surface solution is assured on each iteration by a set of rejection criteria. These criteria (see Appendix C for details) prove to reject the majority of unphysical BRF solutions. Convergence usually occurs after four to five iterations resulting in a computational time of 1 minute to process one spectral band of a SPC cube at 450 m/pixel on a regular computer (i.e., dual 2.66 GHz quad-core processor, 6 GB RAM).
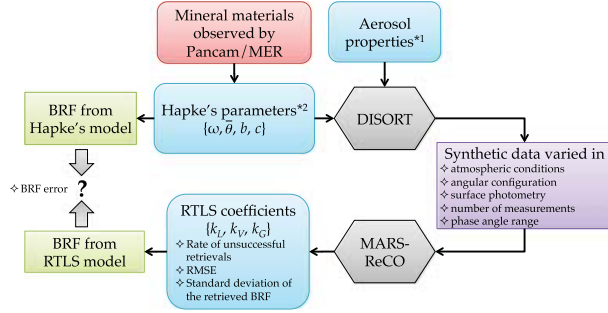
2.2.6.6. Characterizing the Solution

[37] After reaching convergence on iteration m, the quality of the solution is characterized by a series of indicators. First, the root mean square error is computed to express the adequacy between the CRISM measurements and the retrieved BRF model such that

$$RMSE^{(m)} = \sqrt{\frac{1}{N_g} \sum_{j=1}^{N_g} \left(r^{(m)}_j - F^{L(m)}_j k^{L(m)} - F^{V(m)}_j k^{V(m)} - F^{G(m)}_j k^{G(m)} \right)^2},$$
$$(15)$$

[38] Second, we compute the a posteriori variance on the estimated surface reflectance for each geometry $j = 1, \ldots, N_g$ as the trace of the a posteriori covariance matrix $\mathrm{tr}(\mathbf{C}_{\rho p})$ where $\mathbf{C}_{\rho p} = \mathbf{Q} \mathbf{C}_{kp} \mathbf{Q}^T$. Term $\mathbf{Q}$ is the linear operator relating the state vector to the surface BRF values $\rho^{(m)} = \{\rho^{(m)}_1, \ldots \rho^{(m)}_{N_g}\}$ (computed using equation (5)) such that

$$\rho^{(m)} = \mathbf{Q} \mathbf{k}^{(m)}, \quad \mathbf{Q} = \begin{bmatrix} 1 & f^G_1 & f^V_1 \\ & \cdots & \\ 1 & f^G_j & f^V_j \\ & \cdots & \\ 1 & f^G_{N_g} & f^V_{N_g} \end{bmatrix}. \quad (16)$$

Figure 3. Schema of the sensitivity analysis based on synthetic CRISM-like data. *Aerosol properties are provided by *Wolff et al.* [2009]. *Hapke's parameters of the minerals found in the Gusev crater are borrowed from *Johnson et al.* [2006a].

[39] Finally, the a posteriori standard deviation of a predicted BRF photometric curve is

$$\sigma_\rho = \sqrt{\frac{1}{N_g} \text{tr}(\mathbf{C}_{\rho p})}. \qquad (17)$$

[40] In the following, this parameter proves to be an accurate indicator of the quality of the retrieved surface BRF. Indeed, it helps to flag those surface solutions which are wrong but physical and thus more difficult to detect by the rejection and convergence criteria.

3. Sensitivity Analysis

[41] In this section, the capabilities of MARS-ReCO are tested on simulated data following the sensitivity analysis depicted in Figure 3. Such task is achieved at the CRISM spectral band centered at $\lambda = 755.3$ nm where gas absorption is negligible. The present research also aims at studying the correlation of the a posteriori standard deviation σ_ρ with the quality of the retrieved surface reflectances. First, a CRISM-like synthetic data set is generated for test in Section 3.1 based on the optical properties of Martian aerosols and the photometric properties of some surface materials. Second, Section 3.2 evaluates the performance of MARS-ReCO on photometric curves with different angular configurations, atmospheric conditions, and surface photometric properties. Third, the requirements to process CRISM multi-angle data with a limited angular diversity are given in Section 3.3. Fourth, the stability of the inversion performed by MARS-ReCO is studied in Section 3.4. Lastly, the

impact on MARS-ReCO of the uncertainties of the input aerosol content is explored in Section 3.5.

3.1. Synthetic Data Set

[42] The sensitivity analysis is performed on a controlled synthetic data set formed by CRISM-like photometric curves which are simulated in I/F units using DISORT. We consider a coupled atmosphere/surface system that is fed by the scattering properties of Martian dust aerosols from *Wolff et al.* [2009] and by photometric properties of Martian minerals. The reflectances of several surface materials found in the Gusev crater were measured on ground by the Pancam instrument aboard the MER Spirit. These data were fitted by *Johnson et al.* [2006a] to a Hapke's BRDF model with a two-lobed Henyey-Greenstein phase function [*Hapke*, 1993]. In this research, we select four mineral materials, which belong to two endmembers referred by *Johnson et al.* [2006a] to as (i) endmember "Soil", which corresponds to typical soils being dominant at the spatial scale accessible to CRISM, and (ii) endmember "Red rock", which is related to rocky facets with higher anisotropic photometric properties than soils. Table 1 details two different Pancam measurements of the same endmember at 753 nm, the first one corresponding to a brighter sample of the endmember (subindex 1) and the second one belonging to a darker sample (subindex 2). By selecting these photometrically distinct materials, the sensitivity analysis aims at assessing the capabilities of MARS-ReCO against the variability of Martian mineral surfaces.

[43] Based on Table 1, a TOA photometric curve is simulated by DISORT at 753 nm for each combination of the atmospheric/angular configurations summarized in Table 2. Each photometric curve is made of 11 I/F measurements at constant solar zenith angle and varying view zenith angle, thus mimicking the acquisition of targeted observations by CRISM. A single combination of 11 view zenith angles, one for each measurement, is selected for all synthetic photometric curves as the view angle is quite constant for all CRISM targeted observations. By contrast, six solar zenith angles are considered to embrace the angular range in which CRISM works, going from equatorial ($\theta_0 < 60°$) to polar observations ($\theta_0 > 60°$). Four archetypal configurations are selected in terms of relative azimuth according to the typical functioning of MRO, each one linked to a specific couple of φ_1 and φ_2 values. The fourth configuration represents the extreme case when the direction of the Sun and the direction of the MRO flyby are orthogonal ($\varphi_1 = \varphi_2 = 90°$), resulting in the most limited phase angle range. Note that in this extreme configuration half of the angular measurements are identical to the other half due to the symmetry in view zenith angle. As regards atmospheric opacity, a set of nine AOD values

Table 1. Photometric Parameters at 753 nm of the Four Surface Materials Considered in the Sensitivity Analysis

Endmember\Hapke's Parameters at 753 nm	ω	θ	b	c
Soil-1 (Table 4c in *Johnson et al.* [2006a])	0.69	11	0.241	0.478
Soil-2 (Table 6c in *Johnson et al.* [2006a])	0.65	12	0.170	0.547
Red rock-1 (Table 4b in *Johnson et al.* [2006a])	0.83	19	0.450	0.255
Red rock-2 (Table 8b in *Johnson et al.* [2006a])	0.65	14	0.166	0.801

A Hapke's model with a two-lobed Henyey-Greenstein phase function is used. Parameters ω, $\bar{\theta}$, b, and c correspond to the single-scattering albedo, the macroscopic roughness, the asymmetry parameter, and the backward scattering fraction of the phase function, respectively [*Hapke*, 1993]. Note that a bright backscattering highly anisotropic surface corresponds to $\omega \to 1$, $c > 0.5$, and $b \to 1$.

Table 2. Angular and Atmospheric Ranges Encompassed by the TOA Photometric Curves of the Synthetic Data Set[a]

Parameter	Acquisition and Atmospheric Configurations
θ (°)	1 config.: 70, 63.5, 57.5, 52, 46.5, 25, 46.5, 52, 57.5, 63.5, 70
θ_0 (°)	6 config.: 30; 40; 50; 60; 70; 80
φ_1, φ_2 (°)	4 config.: 0, 180; 30, 150; 60, 120; 90, 90
τ_0	9 config.: 0; 0.1; 0.33; 0.5; 1; 1.5; 2; 2.5; 3

[a]Only one configuration is considered in terms of view zenith angle as this angle is quite constant among the 11 images of all CRISM targeted observations. For the central scan, we choose $\theta = 25°$ as this is the typical average value in real CRISM targeted observations.

at 1 μm is considered to test MARS-ReCO under clear and turbid conditions. The resulting synthetic data set contains 216 configurations for each surface material, making a total of 864 CRISM-like photometric curves.

[44] Lastly, noise is added to the synthetic data set to mimic the signal-to-noise ratio of CRISM observations. An additive Gaussian noise with a noise figure of 1/50 is added to each simulated I/F value (i.e., the standard deviation of a given I/F measurement R_j^C being equal to $R_j^C/50$). Note that this noise level is higher than the one claimed by *Murchie et al.* [2007], that is, a signal-to-noise ratio of 450 dB at 750 nm. In this way we assess MARS-ReCO under less favorable and more realistic conditions.

3.2. Study on the Acquisition Geometry, Atmospheric Opacity and Surface Type
3.2.1. MARS-ReCO Performance Based on Built-in Indicators
[45] Each TOA photometric curve in the synthetic data set is compensated for aerosol contribution by MARS-ReCO. In the case of convergence, the corresponding surface RTLS weights $\mathbf{k}_{sol}$ are retrieved. According to the noise attributes of the synthetic data set, each photometric curve $\mathbf{R}^C = \left\{ R_1^C, \ldots, R_j^C, \ldots, R_{Ng}^C \right\}$ is assumed to have a diagonal covariance matrix $\mathbf{C}_C$ with elements $\sigma_j^2 = \left(R_j^C/50 \right)^2$. In order to determinate the intrinsic limitations of MARS-ReCO, we first consider the ideal case in which the exact optical depth (the AOD values used for the data simulation) is known. Accordingly, parameter $\sigma_{\tau_0}^2$ is set to zero. The performance of the surface inversion is illustrated in Figure 4 in terms of (i) unsuccessful retrievals (i.e., the percentage of photometric curves that have been discarded for inversion), (ii) RMSE, and (iii) standard deviation of the retrieved BRF (σ_ρ).

[46] Figure 4(top) illustrates the percentage of unsuccessful retrievals according to atmospheric conditions (set by τ_0), angular configuration (set by θ_0 and $\{\varphi_1,\varphi_2\}$), and type of material. As it can be seen, the rate of unsuccessful retrievals is about 15% for all TOA photometric curves not sampling the solar cross-principal plane ($\varphi_1, \varphi_2 = \{90°, 90°\}$). This specific azimuthal configuration is related to the most limited phase angle range and does not encompass enough angular diversity for a satisfactory inversion. Likewise, unsuccessful retrievals increase significantly for turbid atmospheres and extreme solar zenith angle, reaching a 40% rate of rejection when $\tau_0 \geq 2$ and $\theta_0 \geq 80°$. Regarding the solar angle, the RTLS model becomes less accurate at extreme

illumination conditions due to the divergence of the geometric kernel [*Lucht et al.*, 2000] and the higher anisotropy of surfaces in this angular range. The success of MARS-ReCO is, by contrast, less dependent on the properties of the surface materials. In particular, MARS-ReCO performs slightly worse when dealing with bland materials such as Soil-2, which may be too dark and too isotropic to be accurately separated from the aerosol photometric curve.

[47] Figure 4(middle) illustrates the quality of the fit between the synthetic data set and the TOA reflectance model by means of the RMSE (see equation (15)). Only the successfully inverted photometric curves are considered in this experiment. The RMSE is generally equal to a few tenths of 1% reflectance, and while it logically increases according to solar zenith angle and AOD, it decreases for reduced phase angle ranges. This result is, however, reasonable since photometric curves along the solar cross-principal plane are easier to fit as they do not sample the aerosol photometric curve spanning the solar principal plane ($\varphi_1, \varphi_2 = \{0°, 180°\}$). Contrary to the lower RMSE, the retrieved BRF model in this case is likely to be wrong. Therefore, the RMSE cannot be considered as a reliable indicator of the quality of MARS-ReCO as the surface/atmosphere model can satisfactorily fit a photometric curve while providing a physically incorrect solution. By contrast, the RMSE coherently increases according to solar zenith angle due to the combined effect of a stronger surface anisotropy at extreme angular configurations and the limitations of the RTLS model. Note that inaccuracies at extreme angles also come from small differences between the Hapke's and the RTLS models as well as the use of a plane-parallel radiative transfer code such as DISORT. Lastly, the RMSE also depends slightly on the type of surface, being higher for anisotropic surfaces.

[48] Finally, Figure 4(bottom) explores the average a posteriori standard deviation of the surface photometric curves (σ_ρ) as defined in equation (17). Again, only the successfully inverted photometric curves are considered. The standard deviation is generally lower than 0.1 for favorable conditions and, contrary to the previous indicators, clearly increases according to AOD, solar zenith angle, and limited phase angle range, which typically correspond to the most challenging scenarios.

3.2.2. MARS-ReCO Performance Based on the Pancam Reference
3.2.2.1. BRF Error in the 11 Acquisition Geometries
[49] The accuracy of the retrieved surface BRF is evaluated using the surface data derived from Pancam. Note that these data are used in the simulation of the synthetic data set. This experiment is done exclusively for those photometric curves for which MARS-ReCO converges. We define the BRF error of a given photometric curve (e_ρ) as the average of the difference between (i) the surface photometric curve retrieved by MARS-ReCO in BRF units and (ii) the same curve reconstructed using the Hapke's model and Table 1

$$e_\rho = \frac{100}{Ng} \sum_{j=1}^{Ng} \frac{\left| \rho_j^{\text{MARS-ReCO}} - \rho_j^{\text{Hapke}} \right|}{\rho_j^{\text{Hapke}}}. \quad (18)$$

[50] Figure 5 shows the result of averaging the BRF error of all photometric curves associated to a given AOD, solar
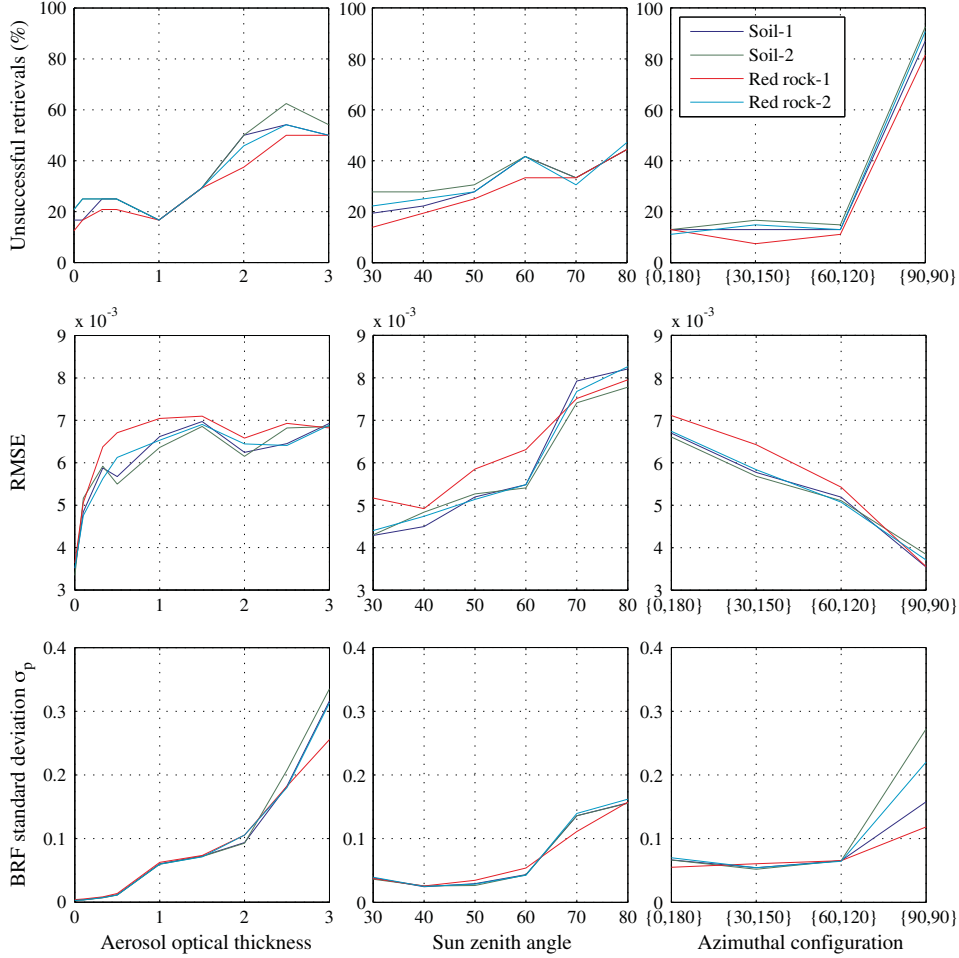
Figure 4. (top) Percentage of unsuccessful retrievals, (middle) RMSE, and (bottom) a posteriori standard deviation of the retrieved BRF for the processed synthetic data set. All parameters are averaged according to the AOD, the solar zenith angle, and the azimuthal configuration that correspond to each synthetic photometric curve. The RMSE and the standard deviation are computed based only on successfully inverted curves.

zenith angle, or azimuthal configuration. As it can be seen, the accuracy of the retrieved BRF decreases under unfavorable conditions, that is, high AOD, extreme solar zenith angle, and limited phase angle range. The average BRF error is lower than 20% when $\tau_0 \leq 1$, $\theta_0 \leq 60°$, and $\varphi_1, \varphi_2 \neq \{90°, 90°\}$ despite the unfavorable configurations of the other parameters (e.g., $e_\rho > 20\%$ when $\tau_0 \leq 1$ and $\theta_0 = 80°$). By contrast, it is important to remark that ranges of validity with higher average BRF errors contain configurations with acceptable accuracies (e.g., for Soil-2, while the average e_ρ is up to 38% when $\tau_0 = 2$, the individual e_ρ is 5.6% for the configuration when $\tau_0 = 2$, $\theta_0 = 30°$, and $\varphi_1, \varphi_2 = \{30°, 150°\}$). Note the high correlation between the BRF error and the a posteriori standard deviation (σ_ρ) in Figure 4(bottom). Lastly, we remark the continuity of the error curves when $\tau_0 = 1.5$. Contrary to the adjacent situations ($\tau_0 = 1$ and $\tau_0 = 2$), this particular aerosol content is not considered in the look-up table, and therefore, the inversion of the associated curves is made after interpolation of the pre-computed atmospheric quantities (see Section 2.2.5). According to results, the performance of MARS-ReCO is robust against this interpolation.

3.2.2.2. BRF Error in the Complete Upper Hemisphere

[51] The capabilities of MARS-ReCO are further validated by evaluating the retrieved surface BRF model out of the 11 acquisition geometries. This time we use a dense angular grid to explore the whole upper hemisphere in view zenith angle and relative phase angle. The evaluation is, however, restricted to the illumination conditions of acquisition (θ_0) as the investigation of other angular ranges becomes unpredictable. Figures 6 and 7 assess a couple of surface models that have been retrieved under varied acquisition conditions. The BRF models are evaluated at the defined angular grid and plotted in polar coordinates, where the radial and angular coordinates correspond to the view zenith angle and the relative azimuth of evaluation, respectively. Note that while the case illustrated in Figure 6 corresponds to very favorable conditions, the examples in Figure 7 are increasingly challenging in terms of AOD, solar zenith angle, azimuthal configuration, and surface anisotropy.

[52] Figure 6 illustrates the evaluation of the retrieved BRF model for a surface made of material Soil-1 in the absence of atmosphere ($\tau_0 = 0$). The Sun position is at $\theta_0 = 30°$ (see yellow star) and the MRO flyby results in a relative
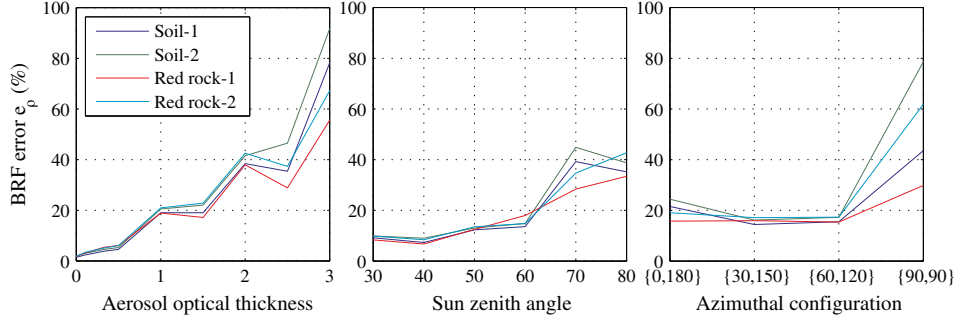
Figure 5. BRF error in percent (e_ρ) between the BRF curve retrieved by MARS-ReCO and the reference data constructed from a Hapke's model fed by Table 1. The plotted BRF errors are the result of averaging each combination of (left) AOD, (center) solar zenith angle, and (right) azimuthal configuration. Only successful retrievals are considered.
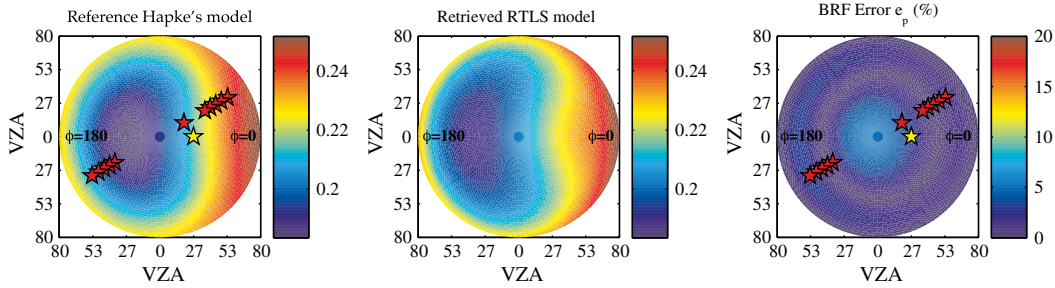
Figure 6. Surface BRF corresponding to material Soil-1 generated using (left) the reference Hapke's model and (center) the RTLS model retrieved by MARS-ReCO from a TOA photometric curve defined by $\tau_0 = 0$ (i.e., no atmospheric effects), $\theta_0 = 30°$, and $\varphi_1, \varphi_2 = \{30°, 150°\}$. (right) BRF error ($e_\rho$) between the BRF calculated from the Hapke's model and that from the RTLS model. Red stars show the geometry of the 11 measurements of the synthetic photometric curve. The Sun position is marked with a yellow star. Note that the backscattering direction is situated at the right-hand side of the plot.

azimuthal angle configuration of $\varphi_1, \varphi_2 = \{30°, 150°\}$. Red stars represent the 11 CRISM-like measurements. This angular configuration results in a phase angle range of acquisition where $g \in [14°, 96°]$. Figure 6(left) shows the surface BRF calculated using the Hapke's model fed by the reference photometric data in Table 1 and evaluated at $\theta_0 = 30°$. Similarly, Figure 6(center) shows the surface BRF calculated using the RTLS model fed by the $\mathbf{k}_{sol}$ retrieved by MARS-ReCO. Figure 6(right) expresses the quality of the retrieval by plotting the relative difference between both BRF data sets. A low error ($e_\rho = 0.8\%$) underlines the compatibility of the RTLS and the Hapke's models even with a few available measurements and despite the additive noise. This result is in agreement with the low BRF standard deviation ($\sigma_\rho = 0.002$) given by MARS-ReCO.

[53] The same experiment is repeated in Figure 7a for a typical atmospheric opacity on Mars, that is, $\tau_0 = 0.5$. Despite the aerosol effects, the BRF error and the standard deviation are very low ($e_\rho = 1.6\%$ and $\sigma_\rho = 0.004$), mainly due to the favorable angular and atmospheric conditions. As it can be seen, MARS-ReCO satisfactorily retrieves a surface model with two scattering lobes in the backward and forward directions. The sole dissimilarity is observed in the forward direction when $\theta \approx 80°$ where the differences between the two surface models become significant.

[54] In Figure 7b, the aerosol contribution is severely increased ($\tau_0 = 2$) to recreate very turbid conditions. This configuration results in a higher BRF error ($e_\rho = 5.6\%$), which is well correlated with a higher standard deviation ($\sigma_\rho = 0.027$). Note that the BRF error is relatively moderate since strong inaccuracies mainly happen at high view zenith angles (errors up to 50%), which are not sampled by the CRISM geometries.

[55] Figure 7c repeats the same experiment with $\tau_0 = 0.5$ and $\theta_0 = 70°$ ($g \in [28°, 130°]$). Although the retrieved backscattering lobe is accurate, the extreme illumination conditions result in a somewhat incorrect forward scattering feature. Nonetheless, similar to Figure 7b, the average BRF error along the 11 geometries is moderate ($e_\rho = 3.0\%$) as well as the associated standard deviation ($\sigma_\rho = 0.011$). Note that the BRF error is expected to increase for higher values of solar zenith angle due to limitations of both surface models.

[56] The experiment in Figure 6 is repeated with $\tau_0 = 0.1$ and $\varphi_1, \varphi_2 = \{90°, 90°\}$, resulting in a very limited phase angle range of acquisition ($g \in [38°, 73°]$). The inversion of this photometric curve is one of the few that converges under this azimuthal configuration [Figure 4(top right)], probably because the rest of acquisition conditions are favorable. Nonetheless, Figure 7d shows that the shape of the retrieved surface model is strongly inaccurate (error up to 80%). This result comes from the restriction of the TOA measurements
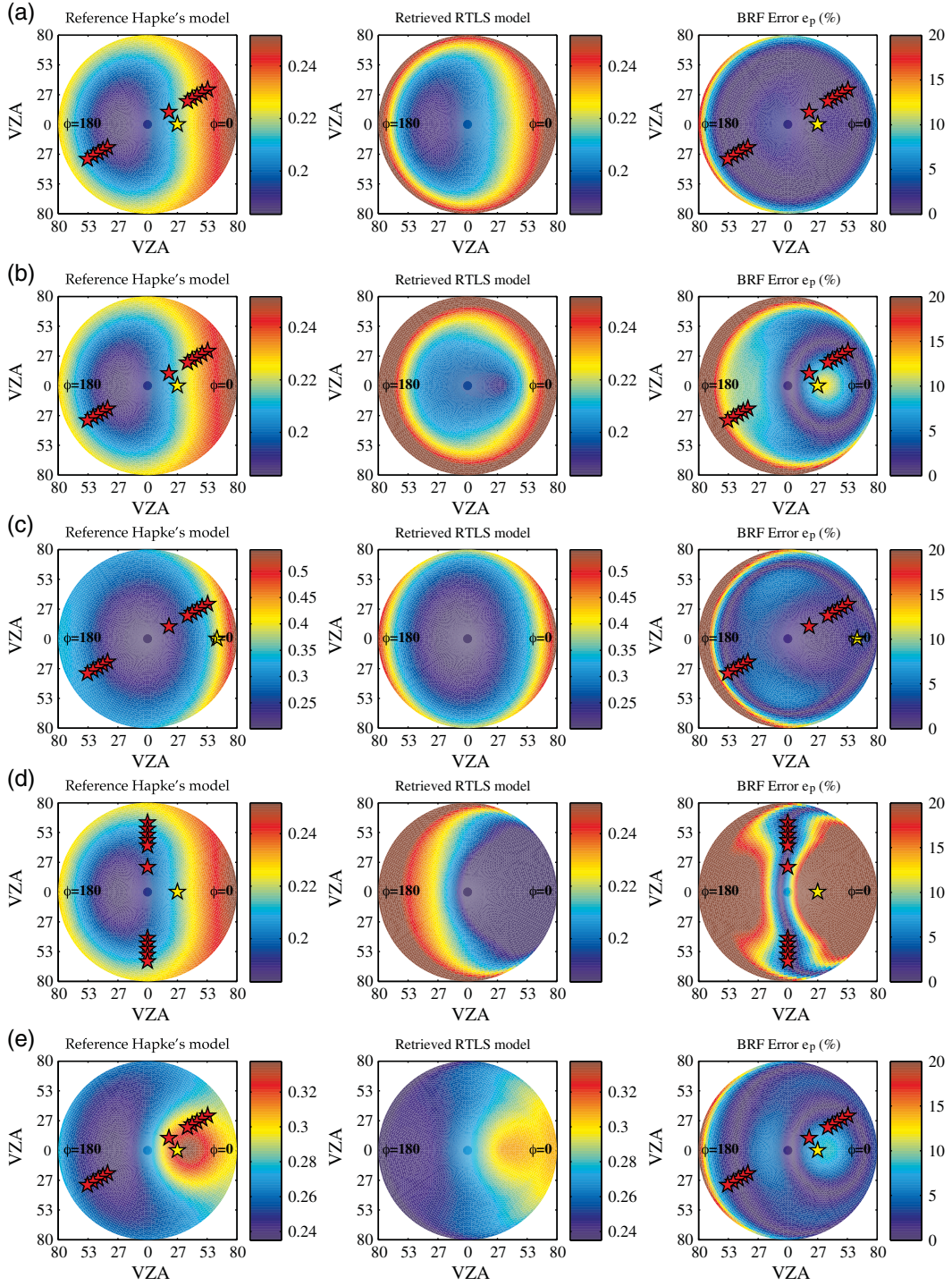
Figure 7. From top to bottom, same as Figure 6 when (a) $\tau_0 = 0.5$, (b) $\tau_0 = 2$, (c) $\tau_0 = 0.5$ and $\theta_0 = 70°$, (d) $\tau_0 = 0.1$ and $\varphi_1, \varphi_2 = \{90°, 90°\}$, and (e) $\tau_0 = 0.5$ and surface made of material Red rock-1.

to the solar cross-principal plane where the main surface scattering features of Soil-1 cannot be sampled. Note, however, that the average BRF error and the standard deviation are quite low ($e_\rho = 1.8\%$ and $\sigma_\rho = 0.003$) as inaccuracies are found out of the 11 sensing geometries. This example highlights the differences between the quality of the retrieved photometric curve, which is quite high in this case, and that of the complete BRF model, which is very poor.

[57] The last experiment summarized in Figure 7e considers $\tau_0 = 0.5$ and material Red rock-1, which is related to a higher albedo, a higher anisotropy, and a higher surface roughness (Table 1). As it can be seen, the retrieved BRF model is rather accurate and reproduces accurately the main narrow backscattering lobe (i.e., the scattering feature in the forward direction of Red rock-1 is smoothed by the surface roughness $\bar{\theta}$), except for a slight underestimation of 7%. The smoothness of narrow

and strong lobes is a typical limitation of the RTLS model [*Roujean et al.*, 1992]. Again, the highest BRF error is obtained in the forward direction for extreme viewing geometries ($\theta > 70°$). This configuration is associated to a low average BRF error and a low standard deviation ($e_\rho = 2.5\%$ and $\sigma_\rho = 0.005$), indicating the goodness of the retrieval.

3.3. Study on Observations with Restricted Geometry

[58] Up to this point MARS-ReCO has been applied to photometric curves made of 11 measurements. Unfortunately, this situation does not correspond to reality since less than 20% of the area encompassed by CRISM targeted observations is typically sensed by more than seven geometries (see Figure 2). The following experiments aim at assessing MARS-ReCO against a reduced number of measurements and thus a restricted geometry.

3.3.1. Number of Angular Measurements and Phase Angle Range

[59] The synthetic data set defined in Section 3.1 is iteratively degraded by removing an increasing number of measurements from each photometric curve. The position of the removed measurements in terms of view zenith angle is chosen randomly. MARS-ReCO is applied to the resulting data set on each iteration until only three measurements are available. Note that the inversion for the RTLS kernel weights with less than three measurements becomes unconstrained. The performance of MARS-ReCO is assessed according to the number of measurements and the phase angle range encompassed by each photometric curve. Note that a high number of measurements within a narrow phase angle range may be less appropriate than few measurements and a broad phase angle range [*Souchon et al.*, 2011].

[60] According to Figure 8(top left), the rate of unsuccessful retrievals remains rather acceptable except for photometric curves with a phase angle range lower than 40°. In this case, photometric curves do not contain enough angular diversity to separate the photometric curve of aerosols from that of the surface, regardless of the number of geometries. Note how the performance of MARS-ReCO decreases for a reduced number of geometries as the inversion becomes progressively unconstrained. However, the number of available geometries is less crucial than the phase angle diversity in terms of convergence.

[61] Figures 8(bottom left) and 8(bottom right) explore the a posteriori standard deviation (σ_ρ) and the error (e_ρ) of the retrieved BRF, respectively. Again, the phase angle range appears as the most critical parameter to perform an accurate atmospheric correction. In fact, Figure 8(bottom right) shows the decrease of the retrieved BRF accuracy for limited phase angle ranges combined with a few available geometries. These unfavorable situations can be detected when processing real CRISM observations based on the a posteriori standard deviation. Indeed, this parameter shows a strong correlation with the BRF error, thus confirming its pertinence as an indicator of the accuracy of the retrieved surface. By contrast, Figure 8(top right) proves that the RMSE is not correlated with the accuracy of MARS-ReCO. For instance, contrary to the BRF error, the RMSE is minimum when only three geometries are available as photometric curves are easier to fit in this case. Lastly, note that the
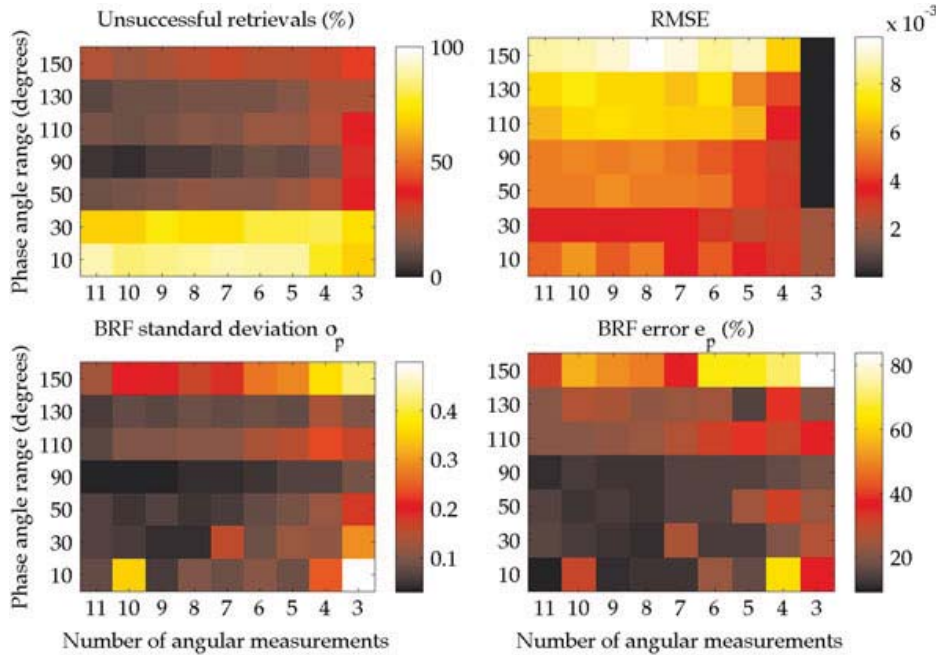
Figure 8. (top left) Percentage of unsuccessful retrievals, (top right) RMSE, (bottom left) a posteriori standard deviation of the retrieved BRF surface σ_ρ, and (bottom right) average BRF error (e_ρ) computed along the acquisition geometries according to the number of measurements and the phase angle range (Δg). The RMSE, BRF error, and parameter (σ_ρ) are computed only for the successfully processed photometric curves. The y axis of the figures is defined such that the row associated to a phase angle range of 110° encompasses the photometric curves within $100° < \Delta g \leq 120°$. Results when $\Delta g = 70°$ and $\Delta g = 170°$ are not shown due to the absence of photometric curves at these configurations.

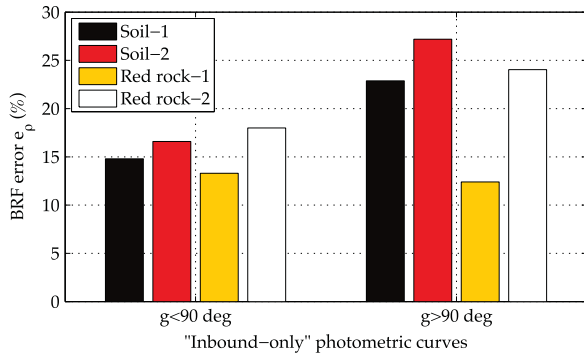rather inaccurate results obtained when dealing with very broad phase angle ranges (larger than 140°) are misleading. In fact, this situation encompasses the most extreme illumination conditions ($\theta_0 > 70°$).

3.3.2. Distribution of the Phase Angle

[62] The previous experiment does not take into account which phase angles are sampled by the photometric curves. Although broad sampled phase angle range are usually beneficial, not all ranges of a given magnitude are equally useful. Furthermore, since the end of 2010, CRISM is acquiring targeted observations without inbound portion due to gimbal stickiness [*Murchie*, 2012]. These restricted range observations sample either small phase angles (when the Sun is "behind" MRO) or large phase angles (when the Sun is "in front" of MRO) while corresponding to similar magnitudes of phase angle range.

[63] In order to assess the performance of MARS-ReCO according to the sampled phase angles, two synthetic data sets are built based on the data set described in Section 3.1. Both data sets mimic the latest restricted range observations by containing photometric curves with only five measurements corresponding to a single mode of azimuth, φ_1 or φ_2 (see Table 1). The first data set simulates no inbound observations sampling small phase angles, while the second one favors larger phase angles. The BRF error at the acquisition geometries e_ρ resulting from the inversion of these two data sets is explored according to the type of material in Figure 9. Two cases are defined to study the sampled phase angles. The first case computes the average BRF error of all "backward" photometric curves ($g \in [0°, 90°]$), while the second case considers all "forward" curves ($g \in [90°, 180°]$). Note that there are approximately 30% less photometric curves in the second case as the phase angle becomes quite small for $\varphi_2 = 120°$ or 90°, especially when solar zenith angle is small.

[64] According to Figure 9, the predominance of aerosol contribution results in larger BRF errors for "forward" photometric curves. Also, the BRF error is larger where there is less signal coming from the surface as it happens for backscattering surface materials when $g \in [90°, 180°]$. Contrarily, the BRF
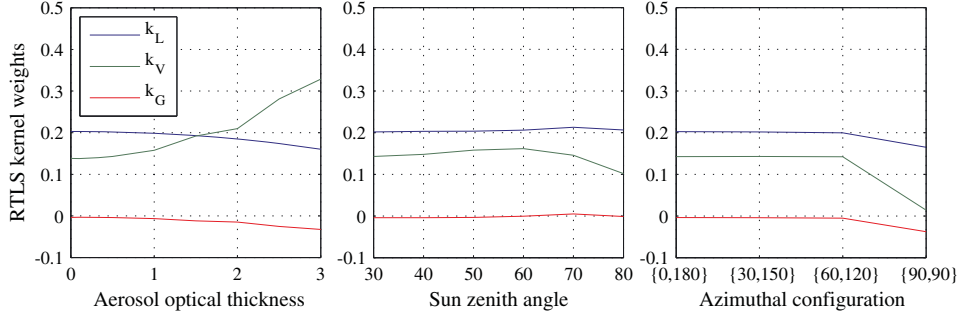
error related to Red rock-1 is larger when $g \in [0°, 90°]$ as this material is forward scattering. The BRF error decreases for large reflectances and sharp scattering lobes (e.g., Red rock-1) as the surface signal is easier to retrieve in this case. In opposite, flat scattering lobes result in higher BRF errors (e.g., Soil-2 obtains a higher error than Soil-1 since the latter has a sharper lobe) even for highly anisotropic materials (e.g., Red rock-2). In conclusion, while the BRF error for no inbound observations is somewhat higher than for complete observations (see Figure 5), it is still reasonable ($e_\rho \approx 20\%$). This result underlines that MARS-ReCO is appropriate to process restricted range CRISM observations provided that five angular measurements are available. In particular, backscattering surfaces are prone to be retrieved more accurately when the outbound images have the Sun in the back (i.e., small phase angles), that is, when MRO in is in the north (south) hemisphere in its descending (ascending) node. Finally, it should be remarked that the retrieved BRF model is likely to be less accurate out of the acquisition geometries than for complete targeted observations.

3.4. Study on the Stability of the Surface Solution

[65] This experiment explores the robustness of MARS-ReCO by assessing the stability of the retrieved surface solution for a set of similar photometric curves. With this aim, MARS-ReCO is run on a set of photometric curves deriving from a particular configuration defined by material Soil-1, $\tau_0 = 0.5$, $\theta_0 = 30°$, and $\varphi_1, \varphi_2 = \{30°, 150°\}$. Figure 10 shows the evolution of the retrieved RTLS kernel weights according to a varying AOD, solar zenith angle, and azimuthal configuration. In Figure 10(left), for instance, the AOD associated to the set of photometric curves varies in contrast to the solar zenith angle and the azimuthal configuration, which remain at their initial values. According to results, the surface BRF models provided by MARS-ReCO for material Soil-1 are quite alike despite the variability encompassed by the data set of study. Only extreme configurations such as $\varphi_1, \varphi_2 = \{90°, 90°\}$ or $\theta_0 = 80°$ result in a significantly different RTLS triplet $\mathbf{k}_{sol}$. As for the aerosol content, Figure 10(left) shows that an increasing AOD results in a slight variation of all RTLS kernel weights (note that the geometric kernel function F^G is much larger than the volumetric one F^V, and therefore, the associated weights k^G are respectively smaller). The increase in k^V is compensated by the decrease in k^G, so the anisotropy of the surface is maintained. This result underlines that two slightly different combinations of the RTLS weights can provide two satisfactory surface fits at the acquisition geometries. Note, however, that when $\tau_0 > 2$ the retrieved BRF models are certainly incorrect.

3.5. Study on the Aerosol Content Uncertainty

[66] Up to now MARS-ReCO has been fed with the exact aerosol content that is used for the data simulation. In reality, however, the actual optical depth of a given observation can be known only with a given uncertainty. *Clancy et al.* [2003] find a ±0.05 uncertainty for retrieved optical depths between 0.20 and 0.50 using EPF observations taken by the Thermal Emission Spectrometer aboard Mars Global Surveyor. *Lemmon et al.* [2004] determine typical uncertainties between ±0.02 and ±0.04 when measuring the AOD with the MER rovers. *Vincendon et al.* [2009] find uncertainties

Figure 9. Average BRF error at the acquisition geometries (e_ρ) for a set of photometric curves without the inbound portion found in CRISM targeted observations. Two classes are defined according to the distribution of the phase angle, those sensing the surface of Mars exclusively (i) in the backward direction ($g \in [0°, 90°]$) and those (ii) in the forward direction ($g \in [90°, 180°]$).

Figure 10. RTLS kernel weights retrieved from a set of photometric curves initially defined by material Soil-1, $\tau_0 = 0.5$, $\theta_0 = 30°$, and $\varphi_1, \varphi_2 = \{30°, 150°\}$. The AOD, solar zenith angle, and azimuthal configuration vary in the left, center, and right figures, respectively.

of ±10% for moderate aerosols loading ($\tau_0(1\mu m) = 0.5$) and of ±20% for high aerosols contribution ($\tau_0(1 \mu m) = 1$) using OMEGA observations. Similarly, *Wolff et al.* [2009] obtain uncertainties of ±10–20% for aerosol depths measured with CRISM EPF data.

[67] The last experiment of the sensitivity analysis investigates the impact of these uncertainties on the MARS-ReCO capabilities. We now consider that the actual optical depth is affected by an unknown additive bias such that $\tau'_0 = \tau_0 + b_{\tau_0}$. According to the studies cited above, the bias affecting aerosol content is modeled with a normal distribution that introduces an average bias of ±15% (standard deviation of 5%). In this way, a vector of 216 different biases b_{τ_0}—negative and positive with different magnitudes—is generated, one for each synthetic photometric curve. The suite of inversions performed in Section 3.2.1 is repeated using the biased optical depths (τ'_0). The error on the latter estimates is considered by setting the parameter characterizing the AOD uncertainty to $\sigma_{\tau_0}^2 = \left(0.15 * \tau'_0\right)^2$ (see Section 2.2.6).

[68] Figure 11 illustrates the inversion quality by means of the typical MARS-ReCO indicators. Only the dependence on aerosol optical depth is shown as the relation between the inversion quality, and all acquisition parameters is very similar to that observed for the ideal case (see Figures 4 and 5). In fact, only the average value of the quality indicators suffers significant variations. In particular, the RMSE

and the BRF error (e_ρ) undergo an increase of 30% and 9%, respectively. This decrease in the quality of the retrieved surface reflectance results in an increase of the evaluated uncertainty of the surface BRF (σ_ρ) by a factor 2. Higher inaccuracies for $\tau_0 = 2$ are explained by the higher bias that affects the photometric curves typically related to the greatest errors (e.g., $\theta_0 = 80°$) in this AOD interval. Likewise, remember that the CRISM-like data are affected by random noise. Lastly, the rate of unsuccessful retrievals is not shown for this experiment as results are very similar to those in Figure 4. Although the rate of successful retrievals decreases due to the error on the AOD estimates, the relaxation introduced in the inversion by considering $\sigma_{\tau_0}^2 \neq 0$ helps MARS-ReCO fitting the TOA photometric curves.

4. Discussion

[69] According to the sensitivity analysis described in the previous section, MARS-ReCO proves to be appropriate to process real CRISM targeted observations. Surface reflectance curves provided by MARS-ReCO are physically plausible and mostly accurate. The few inaccurate surface solutions can be detected by examining the a posteriori standard deviation of the estimated BRF (σ_ρ) provided by MARS-ReCO. This output has proved to be a satisfactory indicator of the quality of the retrieved surface reflectance according to its high correlation with the BRF error. Note that the latter indicator is
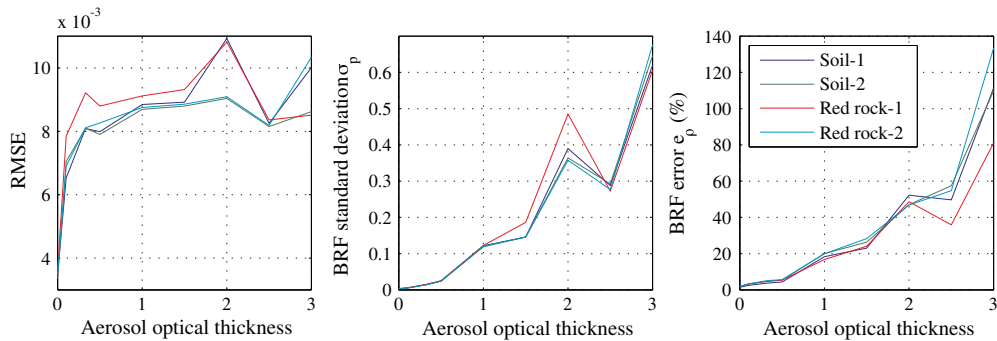
Figure 11. RMSE, a posteriori standard deviation of the retrieved BRF, and BRF error when a 10% uncertainty is considered for the aerosol content estimate. Note the different vertical axis range with respect to Figures 4 and 5.

accessible only if ground truth data are available. Based on the sensitivity analysis, this section establishes the range of conditions over which MARS-ReCO is able to confidently retrieve surface properties from CRISM targeted observations.

[70] Table 3 summarizes the main results obtained by the sensitivity analysis. In particular, retrievals of surface reflectance are possible (unsuccessful retrievals lower than 5%) and relatively accurate (BRF error lower than 20%) when TOA photometric curves are related to (i) an appropriate angular configuration set by a moderate solar zenith angle ($\theta_0 < 70°$) and an azimuthal configuration ensuring a broad phase angle range ($\Delta g \in [40°, 140°]$), and (ii) a surface signal which is significant compared to the aerosol contribution, that is, a moderate AOD ($\tau_0 \leq 1.5$). Accuracy can be increased ($e_\rho < 10\%$) by restricting the validity ranges to $\theta_0 \leq 60°$ and $\tau_0 \leq 0.9$. Furthermore, results show that surfaces combining a low albedo and a low anisotropy (e.g., Soil-2 with $\omega = 0.65$ and $c = 0.17$) lead to slightly worse retrievals (accuracy decrease of 10%). The previous range of conditions is subject to the availability of the aerosol content over CRISM observations. An average decrease of 9% of the quality of the retrieved surface reflectance must be expected for AOD estimates with a 15% error.

[71] In practice, the range of conditions providing inaccurate surface solutions is limited. First, the inversion of CRISM observations with restricted phase angle range (e.g., $\varphi_1, \varphi_2 = \{90°, 90°\}$) is discarded by the criteria of MARS-ReCO (90% of rejection in this case). In this matter, experiments underline that the reflectance accuracy remains acceptable ($e_\rho \lesssim 20\%$) even against a reduced number of angular measurements (down to 5–6 geometries) as long as a broad phase angle range is available ($\Delta g \in [40°, 140°]$). Configurations out of these bounds make the separation between aerosol and surface signals not possible due to the lack of angular diversity, when $\Delta g < 40°$, or the scarcity of available geometries, when $\Delta g > 140°$. Second, opacities on Mars are often rather low ($\tau_0 < 1$ long-ward of one micron [Smith, 2009]). However, precaution must be taken when processing CRISM observations from the high latitudes of Mars as they can be acquired with solar zenith angles around 70°. Besides the limitations of the RTLS surface model at these angles, the plane-parallel approximation used by DISORT may affect the surface retrievals. In this situation (and other unfavorable cases), the a posteriori standard deviation of the estimated BRF (σ_ρ) must be inspected in order to detect incorrect surface retrievals. Experiments prove that surface solutions with $\sigma_\rho \lesssim 0.08$ are related to errors greater than 20%.

[72] It is important to remark that despite a low standard deviation ($\sigma_\rho < 0.08$), the retrieved BRF surface model must be handled with care when it is evaluated out of the CRISM acquisition geometries (Figure 7d). Also, MARS-ReCO has

proved to be stable (variability of ~10% of the retrieved surface model) when dealing with a group of adjacent CRISM-like super-pixels belonging to the same surface material but observed with slightly different geometric configurations.

5. Conclusions

[73] A radiative transfer-based algorithm for atmospheric correction is put forward to retrieve surface reflectance from CRISM multi-angle imagery. The method referred to as MARS-ReCO transforms a set of gas-free TOA radiances, which correspond to the same terrain unit observed at different geometries, into a photometric curve in units of surface reflectance. MARS-ReCO represents a substantial improvement regarding the state of the art in atmospheric correction of Martian data as it considers a non-Lambertian surface along with the photometric curve of the aerosols. The latter data are an input of the proposed technique as well as the aerosol optical depth. Although being based on a radiative transfer model, MARS-ReCO is very fast as it is based on an efficient formulation of the TOA signal and a linear model for the surface reflectivity. In addition, MARS-ReCO integrates a statistical formalism that propagates several uncertainties to the solution, thus providing an accurate indicator of the quality of the retrieved surface reflectance. These statements are confirmed by the sensitivity analysis that is presented in this article and that has proven the validity, the accuracy, and the stability of the surface solutions retrieved from realistic synthetic data (CRISM-like geometric configuration and noise) under realistic conditions (Martian optical depths associated to the typical uncertainties provided by aerosol retrieval methods). This is further proved in the companion article [Fernando et al., 2013] where MARS-ReCO processes real CRISM observations and retrieves surface reflectance curves, which are highly accurate (maximum error of 5%) when compared to in situ measurements.

[74] MARS-ReCO is subject to some limitations when processing CRISM multi-angle data acquired under unfavorable acquisition conditions, that is, turbid atmospheres, extreme illumination conditions, and restricted phase angle ranges. The uncertainties on the surface reflectance retrieved under these situations are, however, quantified by the a posteriori standard deviation provided by MARS-ReCO. It is important to note that the potential of MARS-ReCO to map the photometric properties of the surface of Mars is subject to the degree of overlap among the individual images composing a CRISM targeted observation. In this matter, MARS-ReCO has proved to be robust against observations with restricted geometry such as those acquired by CRISM from late 2010. Furthermore, restricted geometry diversity can be overcome by combining different CRISM observations

Table 3. Performance of MARS-ReCO in Terms of Unsuccessful Retrievals and BRF Error (e_ρ) According to Acquisition Configuration

Convergence and BRF Error	Optical Depth	Solar Zenith Angle	Phase Angle Range
Unsuccessful retrievals < 5%	$\tau_0 \leq 2.0$	$\theta_0 < 70°$	$\Delta g \geq 40°$
Unsuccessful retrievals > 5%	$\tau_0 > 2.0$	$\theta_0 \geq 70°$	$\Delta g < 40°$
$e_\rho < 10\%$, ($\sigma_\rho \lesssim 0.04$)	$\tau_0 \leq 0.9$	$\theta_0 \leq 60°$	$\Delta g < 100°$ [a]
$e_\rho < 20\%$, ($\sigma_\rho \lesssim 0.08$)	$\tau_0 \leq 1.5$	$\theta_0 < 70°$	$\Delta g \in [100°, 140°]$
$e_\rho > 20\%$, ($\sigma_\rho \gtrsim 0.08$)	$\tau_0 > 1.5$	$\theta_0 \geq 70°$	$\Delta g > 140°$

[a]The few photometric curves satisfying $\Delta g < 40°$ that pass the inversion criteria (see in Appendix C) lead to physically plausible surface reflectance curves (low e_ρ) but strongly incorrect BRF models (see Figure 7d).

of the same target acquired under different angular configurations. Eventually, note that this article assesses the performance of MARS-ReCO on gas-free wavelengths. In order to process the whole CRISM spectral range, gaseous contribution must be previously compensated [*McGuire et al.*, 2009; *Douté*, 2009]. In this case, testing must be carried out to evaluate the impact of the uncertainties coming from a faulty gas correction on the retrieved surface reflectance.

[75] One major advantage of MARS-ReCO is that its look-up table can be easily adapted to accommodate different scenarios. In this article, the look-up table considers only mineral aerosols, making MARS-ReCO suitable to process most CRISM observations acquired over the equatorial regions of Mars. Future versions of the look-up table may, however, consider other atmospheric situations such as the presence of water ice aerosols, mineral aerosols with different grain size, or even gases. Further testing should be performed to test the performance of MARS-ReCO in this case. Likewise, limitations found at extreme zenith angles may be mitigated using a look-up table calculated by a radiative transfer code considering the sphericity of Mars.

[76] Further research will be conducted on the exploitation of the complete surface reflectance model retrieved by MARS-ReCO to calculate directional-hemispherical albedos of the surface as it is done with in situ measurements in *Bell et al.* [2008]. Also, we will address the processing of the whole spectral dimension of CRISM. The resulting increase of the input data, together with the consideration of appropriate techniques, may allow us to retrieve simultaneously the surface BRF and the aerosol optical depth as it is done by *Lyapustin et al.* [2011b].

Appendix A: Green's Function Method for the Radiative Transfer Problem

[77] *Lyapustin and Knyazikhin* [2001] address the use of the Green's function method for the radiative transfer problem. The surface is considered to be non-Lambertian and spatially homogeneous, and the atmosphere is vertically stratified with a plan parallel geometry and τ_0 being the integrated optical depth. The atmosphere is illuminated at the TOA by a quasi collimated solar beam of flux πS with incident direction $s_0 = (\theta_0, 0)$. The direction of radiation propagation within the atmosphere is noted $s = (\theta, \varphi)$. The vertical axis z points downward so that downward directions of propagation ($\mu > 0$) are indicated by a plus sign ($+$) while the upward direction ($\mu < 0$) corresponds to a minus sign ($-$). The wavelength of measurement of the sensor λ is omitted for clarity. The method is based on the additive properties of the radiative transfer equation and on three ideas.

1. First, the total radiance at a given level of optical depth τ and direction of propagation s is decomposed into the radiance corresponding to the photons that never interacted with the surface and a term corresponding to the radiance carried by all other photons

$$L(\tau; s_0, s) = D(\tau; s_0, s) + J(\tau; s_0, s), \qquad (A1)$$

where the first term depends only on the properties of the atmosphere and obeys the radiative transfer equation with

the boundary conditions $D_+(0) = 0$ and $D(\tau_0) = 0$.

2. Second, the determination of the radiative response of the atmosphere to a given field of upward radiance at the surface-atmosphere interface $L_-(\tau_0, s')$ requires the calculation of the atmospheric response $G^d(\tau; s', s)$ if the atmosphere is illuminated from below with an elementary collimated flux beam $\pi S = 1$ in the direction s'. This diffuse Green's function $G^d(\tau; s', s)$ is a solution to the radiative transfer problem adjoint to the standard radiative transfer equation which solution is $D(\tau; s_0, s)$. By adjoint, we mean reversing the order of the atmospheric layers ($\tau \to \tau_0 - \tau$) but with the same boundary conditions, that is, $G^d_+(0) = 0$ and $G^d_+(\tau_0) = 0$. Similar to $D(\tau; s_0, s)$, the term $G^d(\tau; s', s)$ depends only on the properties of the atmosphere. We define the operator

$$\hat{\Gamma}_{\tau,s} L_- = \int_{\Omega^-} ds' \, G^d\left(\tau, s', s\right) L_-\left(\tau_0, s'\right), \qquad (A2)$$

which transforms $L_-(\tau_0, s')$ into the atmospheric response.

3. Third, the radiance field $J(\tau; s_0, s)$ is considered as a series of converging terms $J^{(j)}(\tau; s_0, s)$ that quantify the radiative flux of photons which have undergone a number j of surface-atmosphere round trips. On the surface-atmosphere interface, it is possible to formalize the physical interaction that binds a term $j - 1$ to the next j such that

$$J^{(j)}_-(\tau_0) = \hat{R}\hat{\Gamma}^+_{\tau_0} J^{(j-1)}_-(\tau_0), \qquad (A3)$$

and, at this level, the series converges to

$$J_-(\tau_0) = \sum_{j \geq 1} J^{(j)}_-(\tau_0) = \left[\hat{I} - \hat{R}\cdot\Gamma^+_{\tau_0}\right]^{-1} \hat{R} L^{(0)}_+(\tau_0), \qquad (A4)$$

the zeroth-order illumination of the surface being

$$L^{(0)}_+(\tau_0 s) = \pi S e^{-\tau_0/\mu_0}\delta(s - s_0) + D(\tau_0; s_0, s), \qquad \mu > 0. \quad (A5)$$

[78] In all cases, the operator $\hat{R}$ expresses the reflection by the surface of a downward radiance field into a upward radiance field

$$J^{(j)}_-(\tau_0) = \hat{R}J^{(j-1)}_+(\tau_0) = \int_{\Omega^+} ds' \, \rho\left(s', s\right)\mu' J^{(j-1)}_+\left(\tau_0, s'\right). \quad (A6)$$

[79] Transferring the total radiance exiting the surface to the TOA and adding the additive contribution of the latter, the TOA radiation measured by the instrument becomes

$$L(\tau = 0; s_0, s) = D(0; s_0, s) + \hat{\Gamma}^-_{0,s}\left[\hat{I} - \hat{R}\cdot\Gamma^+_{\tau_0}\right]^{-1} \hat{R} L^{(0)}_+(\tau_0), \quad (A7)$$
$$\mu < 0.$$

A1. Practical Resolution

[80] In order to achieve the calculation, it is necessary to calculate each term $J^{(j)}_-(\tau_0; s)$, $j \geq 1$ using equation (A3) resulting in a quadruple numerical integration. In the case of a surface and/or atmosphere high albedo, the series can be long to converge and the number of terms required in the summation becomes important. Two main assumptions

become therefore necessary to circumvent the prohibitive computation time in this case.

1. After a sufficiently large number of atmosphere-surface round trips, two successive terms of the series become proportional; that is, the angular structure of the radiance field is preserved at the interface ($\tau = \tau_0$), the absolute level becoming weaker and weaker:

$$J_-^{(j+1)}(\tau_0) = \hat{R}\hat{\Gamma}_{\tau_0}^+ J_-^{(j)}(\tau_0) \simeq \eta J_-^{(j)}(\tau_0). \quad (A8)$$

For many natural surfaces that are reasonably anisotropic, this number is very small $j = 2$. Then we only need to calculate the terms $J_-^{(j)}(\tau_0), j = 2, 3$ with equation (A3) starting with

$$J_-^{(1)}(\tau_0;s) = S\mu_0 e^{-\tau_0/\mu_0}\rho(s_0,s)$$
$$+ \frac{1}{\pi}\int_{\Omega^+} ds' \rho(s',s)\mu' D(\tau_0;s_0,s'). \quad (A9)$$

Quantity $\eta \simeq \frac{J_-^{(3)}(\tau_0;s)}{J_-^{(2)}(\tau_0;s)}$ can be now evaluated, allowing a simplified expression of the upward radiance field requiring the computation of only two successive quadruple integrations

$$J_-(\tau_0;s) = J_-^{(1)}(\tau_0;s) + \frac{J_-^{(2)}(\tau_0;s)}{1-\eta}. \quad (A10)$$

2. Assuming that radiation is enough isotropic so that multiple surface-atmosphere reflections occur according to a Lambertian law, factor η is the product of two bi-hemispherical albedos $\eta = c_0\rho_0$, the surface and atmospheric albedos (ρ_0 and c_0) being

$$\rho_0 = \frac{1}{\pi} \cdot \int_{\Omega^-} ds'\mu' \int_{\Omega^+} ds \cdot \rho(s,s'), \quad (A11)$$

$$c_0 = \frac{1}{\pi} \cdot \int_{\Omega^+} ds'\mu' \int_{\Omega^-} ds G^d(\tau_0;s,s').$$

[81] The resolution proceeds with the simplification of term $J_-^{(2)}(\tau_0;s) = \hat{R}\hat{\Gamma}_{\tau_0}^+ J_-^{(1)}(\tau_0;s)$, which is the diffuse and direct solar illumination reflected once by the surface, then undergoing one surface-atmosphere round trip. As the first diffuse contribution is already a slowly changing function with respect to direction, the angular structure is conserved in the operation which reduces to a multiplication by η. The second contribution can also be approximated but less drastically. This step gives the final expression for the upward radiance rising at the surface-atmosphere interface

$$J_-(\tau_0;s) = S\mu_0 e^{-\tau_0/\mu_0}\left[\rho(s_0,s) + \frac{c_0\rho_1(s)\rho_2(s_0)}{1-c_0\rho_0}\right]$$
$$+ \frac{1}{\pi[1-c_0\rho_0]}\int_{\Omega^+} ds'\rho(s',s)\mu' D(\tau_0,;s_0,s'), \quad (A12)$$

where

$$\rho_1(s) = \frac{1}{2\pi}\int_{\Omega^+} ds'\rho(s',s), \quad \rho_2(s_0) = \frac{1}{2\pi}\int_{\Omega^-} ds'\rho(s_0,s'). \quad (A13)$$

[82] The last step consists in transferring the radiance to the TOA, thanks to the direct and diffuse term of the Green's function as it is done in equations (1)–(4).

Appendix B: Ross-Thick and Li-Sparse Kernels

[83] The volumetric or Ross-Thick kernel is a single-scattering approximation of radiative transfer theory consisting of a Lambertian background and a layer of small scatterers with uniform angle distribution and equal transmittance and reflectance [*Roujean et al.*, 1992]. The form of this kernel, normalized to zero for $\theta_0 = 0°$, $\theta = 0°$, is

$$f_V(\theta_0,\theta,g) = \frac{(\pi/2 - g)\cos g + \sin g}{\cos\theta_0 + \cos\theta} - \frac{\pi}{4}. \quad (B1)$$

[84] The geometric or Li-Sparse kernel assumes a sparse ensemble of randomly located spheroids casting shadows on the background, which is assumed Lambertian [*Wanner et al.*, 1995]. This geometric term is given by the proportions of sunlit and shaded scene components in a scene consisting of randomly located spheroids of height-to-center-of-crown h and crown vertical-to-horizontal radius ratio b/r. For CRISM processing, we take $b/r = 1$ and $b/r = 2$ as it is done for MODIS processing [*Lucht et al.*, 2000]. If the sunlit component is simply assumed to vary as $1/\cos\theta_0$, the kernel takes on the reciprocal form

$$f_G(\theta_0,\theta,\varphi) = O(\theta_0,\theta,\varphi) - \sec\theta'_0 - \sec\theta'$$
$$+ \frac{1}{2}\left(1 + \cos g'\right)\sec\theta'_0\sec\theta', \quad (B2)$$

where

$$O = \frac{1}{\pi}(t - \sin t\cos t)\left(\sec\theta'_0 + \sec\theta'\right),$$
$$\cos t = \frac{h}{b}\frac{\sqrt{D^2 + \left(\tan\theta'_0\tan\theta'\sin\varphi\right)^2}}{\sec\theta'_0 + \sec\theta'},$$
$$D = \sqrt{\tan^2\theta'_0 + \tan^2\theta' - 2\tan\theta'_0\tan\theta'\cos\varphi}, \quad (B3)$$
$$\cos g' = \cos\theta'_0\cos\theta' + \sin\theta'_0\sin\theta'\cos\varphi,$$
$$\theta_0 = \tan^{-1}\left(\frac{b}{r}\tan\theta_0\right), \theta' = \tan^{-1}\left(\frac{b}{r}\tan\theta\right).$$

Appendix C: Rejection and Convergence Criteria

[85] The quality of the surface solutions provided by MARS-ReCO is assured by the following set of rejection criteria adopted from *Lyapustin et al.* [2012]:

1. Before inversion, we check if the photometric curve to be processed satisfies a minimum phase angle sampling, namely, $\max(g_j) - \min(g_j) \geq 20°$, $\forall j \in [1, N_g]$. Inversion is aborted otherwise. Additionally, MARS-ReCO is run only if there are at least three angular measurements as the inversion problem becomes unconstrained otherwise (note the three unknown variables **k**).

2. After retrieving the surface solution $\mathbf{k}^{(n+1)}$ on iteration n, the angular measurements R_j^C that satisfy $\left| R_j^C - R_j^{(n+1)} \right| > 4\sigma_{Rj} = 4\sqrt{C_{pr}^{jj}}$ are excluded. The inversion is restarted on iteration $n+1$ with a reduced number of geometries. Note that σ_{Rj} is the a posteriori 1σ error bar on the modeled TOA reflectance for each geometry. Testing proved that a 4σ threshold is a good trade-off between rejection of wrong solutions and limitations of the inversion method. This criterion is especially useful for challenging CRISM observations such as those acquired over the polar regions or under turbid atmospheric conditions.

3. The physical sense of the retrieved kernel weights $\mathbf{k}^{(n+1)}$ is verified by checking that the associated surface albedo $q^{(n+1)}(\theta_0)$ is positive and lower than unity when $\theta_0 = 15°$, $45°$, $60°$. The inversion of the current photometric curve is aborted otherwise.

[86] At the end of each iteration, the retrieved surface solution is evaluated for convergence by the following convergence criterion:

1. The quality of the derived surface BRF is assessed by a confidence index that is initially low (*flag* = 0, when $n = 0$). The retrieved solution $\mathbf{k}^{(n+1)}$ obtained on iteration n is compared with the previous solution $\mathbf{k}^{(n)}$ as follows | $q^{(n+1)}(\theta_0) - q^{(n)}(\theta_0)| < 0.001$, where $\theta_0 = 15°$, $45°$, $60°$. Each time a new retrieval agrees with the previous solution according to this criterion, *flag* is increased by 1 and the inversion is repeated on next iteration $n+1$ using $\mathbf{k}^{(n+1)}$. The retrieval is considered to be reliable when *flag* = 4. This criterion is useful for CRISM polar observations for which the nonlinear term R^{nl} becomes larger due to the high brightness of the surface and the extreme acquisition geometry.

C1. Notation

C1.1. Spectral and Directional Parameters

θ, θ_0:   view and solar zenith angle
μ, μ_0:   cosine of view and solar zenith angle
φ, g: view-sun relative azimuth and phase angle
s, s_0:   view and sun directions defined by (θ,φ) and (θ_0,φ_0). In this work, $\varphi_0 = 0°$
λ: wavelength

C2. Atmospheric Parameters

$\tau_0(\lambda)$:   aerosol optical depth
$c_0(\lambda)$:   spherical albedo of the atmosphere
$G^d(s_0,s,\lambda)$:   diffuse Green's function of the atmosphere
$D(s_0,s,\lambda)$, $R^D(s_0,s,\lambda)$:   atmospheric reflected path radiance and reflectance
$D_s(s_0,s,\lambda)$:   path radiance incident on the surface
$F_s(s_0,\lambda)$, $F_s^d(s_0,\lambda)$:   direct and diffuse radiative fluxes incident on the surface
$F^{Down}(s_0,\lambda)$, $F^{Up}(s_0,\lambda)$:   downwelling and upwelling radiative fluxes at the surface
$L_s(s_0,s,\lambda)$, $L_s^d(s_0,s,\lambda)$:   direct and diffuse upwelling radiance after surface reflection
$\alpha(s_0,\lambda)$:   multiple reflection factor

C3. Top-of-atmosphere Parameters

$I(s_0,s,\lambda)/F(s_0,\lambda)$:   ratio of measured intensity to solar flux
$L(s_0,s,\lambda)$, $R(s_0,s,\lambda)$:   gas-free radiance and reflectance
$\pi S(s_0,\lambda)$:   extraterrestrial solar spectral irradiance

C4. Surface-related Parameters

$\rho(s_0,s,\lambda)$:   bidirectional reflectance factor
$q(s_0,\lambda)$:   directional-hemispherical surface albedo
$f_G(s_0,s,\lambda)$, $f_V(s_0,s,\lambda)$:   RTLS geometric and volumetric kernels
$\mathbf{k} = \{k^L(\lambda), k^G(\lambda), k^V(\lambda)\}$:   weights for the RTLS kernels

C5. Inversion Parameters

$\mathbf{k}_{sol}$:   weights providing the best fit between the model and the CRISM measurements
$\{F^L, F^G, F^V\}$:   multiplicative factors for the kernel weights
$R^{nl}(\mu_o,\mu)$:   nonlinear term comprising the surface dependence of the TOA reflectance
$r(s_0,s,\lambda)$:   reduced measurements such that $r = R - R^D - R^{nl}$
$\mathbf{C}_C$, $\mathbf{C}_{\tau_0}$, $\mathbf{C}_k$, $\mathbf{C}_r$:   covariance matrix of the CRISM measurements, the AOD estimate, the RTLS weights, and the reduced measurements
$\mathbf{C}_{pr}$, $\mathbf{C}_{pk}$, $\mathbf{C}_{p\rho}$:   a posteriori covariance matrix of the reduced measurements, the RTLS weights, and the retrieved BRF
RMSE: root mean square error between the sensed and the modeled TOA reflectances
σ_ρ: a posteriori standard deviation of a retrieved photometric curve in BRF units
e_ρ: relative error of the retrieved BRF photometric curve as regards the synthetic data

References

Barlow, N. (2008), *Mars: An Introduction to its Interior, Surface and Atmosphere*, Cambridge University Press, Cambridge, U.K., doi:10.1017/CBO9780511536069.

Bell, J. F., III, M. S. Rice, J. R. Johnson, and T. M. Hare (2008), Surface albedo observations at Gusev Crater and Meridiani Planum, Mars, *J. Geophys. Res.*, *113*(E06S18), doi:10.1029/2007JE002976.

Brown, A. J., and M. J. Wolff (2009), Atmospheric modeling of the Martian polar regions: One Mars year of CRISM EPF observations of the south pole, in *Lunar and Planetary Science Conference*, 1675.

Clancy, R. T., and S. W. Lee (1991), A new look at dust and clouds in the Mars atmosphere: Analysis of emission-phase-function sequences from global Viking IRTM observations, *Icarus*, *93*, 135–158.

Clancy, R. T., M. J. Wolff, and P. R. Christensen (2003), Mars aerosol stud-
ies with the MGS TES emission phase function observations: Optical
depths, particle sizes, and ice cloud types versus latitude and solar longi-
tude, *J. Geophys. Res.*, *108*(E9), 5098, doi:10.1029/2003JE002058.
Cull, S., R. E. Arvidson, M. Mellon, S. Wiseman, R. Clark, T. Titus, R. V.
Morris, and P. McGuire (2010), Seasonal H2O and CO2 ice cycles at the
Mars Phoenix landing site: 1. Prelanding CRISM and HiRISE observations,
J. Geophys. Res., *115*(E00D16), doi:10.1029/2009JE003340.
Diner, D. J., J. V. Martonchik, R. A. Kahn, B. Pinty, N. Gobron, D. L. Nelsonc,
and B. N. Holben (2005), Using angular and spectral shape similarity con-
straints to improve MISR aerosol and surface retrievals over land, *Remote
Sens. Environ.*, *94*, 155–171, doi:10.1016/j.rse.2004.09.009.
Douté, S. (2009), Retrieving Mars surface reflectance from OMEGA/MEX
imagery, in *IEEE Workshop on Hyperspectral Image and Signal Proces-
sing: Evolution in Remote Sensing*.
Douté, S., and X. Ceamanos (2010), Retrieving Mars aerosol optical depth
from CRISM/MRO imagery, in *IEEE Workshop on Hyperspectral Image
and Signal Processing: Evolution in Remote Sensing*, Reykjavik.
Drossart, P., J. Rosenqvist, S. Erard, Y. Langevin, J.-P. Bibring, and M.
Combes (1991), Martian aerosol properties from the Phobos/ISM experi-
ment, *Ann. Geophys.*, *9*(11), 754–760.
Erard, S., J. Mustard, S. Murchie, and J.-P. Bibring (1994), Martian aerosols:
Near-infrared spectral properties and effects on the observation of the
surface, *Icarus*, *111*, 317–337.
Fernando, J., X. Ceamanos, F. Schmidt, S. Douté, P. Pinet, and Y. Daydou
(2013), Surface reflectance of Mars observed by CRISM/MRO: 2. Esti-
mation of surface photometric properties in Gusev Crater and Meridiani
Planum, *J. Geophys. Res.*, *118*, doi:10.1029/2012JE004194, in press.
de Grenier, M., and P. C. Pinet (1995), Near-opposition Martian limb-
darkening: quantification and implication for visible-near-infrared
bidirectional reflectance studies, *Icarus*, *115*, 354–368, doi:10.1016/j.
icarus.2008.05.022.
Guanter, L., L. Alonso, and J. Moreno (2005), A method for the surface
reflectance retrieval from PROBA/CHRIS data over land: Application
to ESA SPARC campaigns, *IEEE Trans. Geosci. Remote Sens.*, *43*(12),
doi:10.1109/TGRS.2005.857915.
Hapke, B. (1993), *Theory of Reflectance and Emittance Spectroscopy*, pp.
2908–2917, Cambridge University Press, Cambridge, U. K.
Jehl, A., et al. (2008), Gusev photometric variability as seen from orbit by
HRSC/Mars-express, *Icarus*, *197*, 403–428.
Johnson, J. R., W. M. Grundy, M. T. Lemmon, J. F. Bell III, M. J. Johnson,
et al. (2006a), Spectrophotometric properties of materials observed by
Pancam on the Mars Exploration Rovers: 1. Spirit, *J. Geophys. Res.*,
111(E02S14), doi:10.1029/2005JE002494.
Johnson, J. R., et al. (2006b), Spectrophotometric properties of materials
observed by Pancam on the Mars Exploration Rovers: 2. Opportunity,
J. Geophys. Res., *111*(E12S16), doi:10.1029/2006JE002762.
Korablev, O., V. Moroz, E. Petrova, and A. Rodin (2005), Optical proper-
ties of dust and the opacity of the Martian atmosphere, *Adv. Space Res.*,
35(1), 21–30, doi:10.1016/j.asr.2003.01.061.
Langevin, Y., F. Poulet, J.-P. Bibring, and B. Gondet (2005), Sulfates in the
north polar region of Mars detected by OMEGA/Mars Express, *Science*,
307(5715), 1584–1586, doi:10.1126/science.1109091.
Lemmon, M. T., et al. (2004), Atmospheric imaging results from the Mars
Exploration Rovers: Spirit and Opportunity, *Science*, *306*, 1753–1756,
doi:10.1126/science.1104474.
Lucht, W., C. B. Schaaf, and A. H. Strahler (2000), An algorithm for the re-
trieval of albedo from space using semiempirical BRDF models, *IEEE
Trans. Geosci. Remote Sens.*, *38*(2), 977–998.
Lyapustin, A., Y. Wang, I. Laszlo, R. Kahn, S. Korkin, L. Remer, R. Levy,
and J. S. Reid (2010), Analysis of snow bidirectional reflectance from
ARCTAS spring-2008 campaign, *Atmos. Chem. Phys.*, *10*, 4359–4375,
doi:10.5194/acp-10-4359-2010.
Lyapustin, A., and Y. Knyazikhin (2001), Green's function method for the
radiative transfer problem. I. Homogeneous non-Lambertian surface,
Appl. Opt., *40*(21), 3495–3501.
Lyapustin, A., J. Martonchik, Y. Wang, and I. Laszlo (2011a), Multiangle
implementation of atmospheric correction (MAIAC): 1. Radiative transfer
basis and look-up tables, *J. Geophys. Res.*, *116*(D03210), doi:10.1029/
2010JD014985.
Lyapustin, A., and Y. Wang (2005), Parameterized code SHARM-3D for
radiative transfer over inhomogeneous surfaces, *Appl. Opt.*, *44*(35),
7602–7610, doi:10.1364/AO.44.007602.
Lyapustin, A., Y. Wang, I. Laszlo, R. A. Kahn, S. Korkin, et al. (2011b),
Multiangle implementation of atmospheric correction (MAIAC): 2. Aerosol
algorithm, *J. Geophys. Res.*, *116*(D03211), doi:10.1029/2010JD014986.
Lyapustin, A. I. (1999), Atmospheric and geometrical effects on land surface
albedo, *J. Geophys. Res.*, *104*(D4), 4127–4143.
Lyapustin, A. I., Y. Wang, I. Laszlo, T. Hilker, F. G. Hall, P. J. Sellers, C. J.
Tucker, and S. V. Korkin (2012), Multi-angle implementation of multi-

atmospheric correction for MODIS (MAIAC): 3. Atmospheric correction,
Remote Sens. Environ., doi:10.1016/j.rse.2012.09.002.
Martonchik, J. V. (1994), Retrieval of surface directional reflectance proper-
ties using ground level multiangle measurements, *Remote Sens. Environ.*,
50, 303–316.
Martonchik, J. V., R. A. Kahn, and D. J. Diner (2009), Retrieval of aerosol
properties over land using MISR observations, in *Satellite Aerosol Remote
Sensing Over Land*, pp. 267–293, Springer Praxis Books, Heidelberg.
McGuire, P. C., et al. (2009), An improvement to the volcano-scan algo-
rithm for atmospheric correction of CRISM and OMEGA spectral data,
Planet. Space Sci., *57*, 809–815, doi:10.1016/j.pss.2009.03.007.
McGuire, P. C., M. J. Wolff, M. D. Smith, R. E. Arvidson, S. L. Murchie,
et al. (2008), MRO/CRISM retrieval of surface Lambert Albedos for
multispectral mapping of Mars with DISORT-based radiative transfer
modeling: Phase 1—Using historical climatology for temperatures,
aerosol optical depths, and atmospheric pressures, *IEEE Trans. Geosci.
Remote Sens.*, *46*(12), 4020–4040, doi:10.1109/TGRS.2008.2000631.
Murchie, S. (2012), CRISM on MRO—Instrument and investigation over-
view, in *MRO/CRISM Data Users' Workshop*, The Woodlands, TX.
Murchie, S., et al. (2007), Compact Reconnaissance Imaging Spectrometer
for Mars (CRISM) on Mars Reconnaissance Orbiter (MRO), *J. Geophys.
Res.*, *112*(E05S03), doi:10.1029/2006JE002682.
Nicodemus, F. E., J. C. Richmond, J. J. Hsia, I. W. Ginsberg, and T. Limperis
(1977), Geometrical considerations and nomenclature for reflectance,
National Bureau of Standards, *160*.
Ockert-Bell, M. E., J. F. Bell III, J. B. Pollack, C. P. McKay, and F. Forget
(1997), Absorption and scattering properties of the Martian dust in the
solar wavelengths, *J. Geophys. Res.*, *102*(E4), 9039–9050.
Pinet, P., and C. Rosemberg (2001), Regional photometry and spectral
albedo of the eastern hemisphere of Mars in the 0.7–1 micron domain,
in *Lunar and Planetary Science Conference*, 1640.
Roujean, J.-L., M. Leroy, and P.-Y. Deschamps (1992), A bidirectional re-
flectance model of the Earth's surface for the correction of remote sensing
data, *J. Geophys. Res.*, *97*(D18), 20,455–20,468, doi:10.1029/
92JD001411.
Schaaf, C. B., et al. (2002), First operational BRDF, albedo nadir reflectance
products from MODIS, *Remote Sens. Environ.*, *83*, 135–148.
Smith, M. D. (2009), THEMIS observations of Mars aerosol optical depth
from 2002–2008, *Icarus*, *202*(2), 444–452, doi:10.1016/j.icarus.2009.
03.027.
Smith, M. D., M. J. Wolff, R. T. Clancy, and S. L. Murchie (2009), Com-
pact Reconnaissance Imaging Spectrometer observations of water vapor
and carbon monoxide, *J. Geophys. Res.*, *114*(E00D03), doi:10.1029/
2008JE003288.
Souchon, A. L., P. C. Pinet, S. D. Chevrel, Y. H. Daydou, D. Baratoux, K.
Kurita, M. K. Shepard, and P. Helfenstein (2011), An experimental study
of Hapke's modeling of natural granular surface samples, *Icarus*, *215*,
313–331, doi:10.1016/j.icarus.2011.06.023.
Stamnes, K., S.-C. Tsay, W. Wiscombe, and K. Jayaweera (1988),
Numerically stable algorithm for discrete-ordinate-method radiative transfer
in multiple scattering and emitting layered media, *Appl. Opt.*, *27*(12),
2502–2509.
Tarantola, A. (2005), *Inverse Problem Theory and Methods for Model
Parameter Estimation*, Society for Industrial and Applied Mathematics,
Philadelphia.
Tomasko, M. G., L. R. Doose, M. Lemmon, P. H. Smith, and E. Wegryn
(1999), Properties of dust in the Martian atmosphere from the Imager
on Mars Pathfinder, *J. Geophys. Res.*, *104*, 8987–9008.
Vincendon, M., Y. Langevin, F. Poulet, J.-P. Bibring, and B. Gondet
(2007), Recovery of surface reflectance spectra and evaluation of the
optical depth of aerosols in the near-IR using a Monte Carlo approach:
Application to the OMEGA observations of high-latitude regions of Mars,
J. Geophys. Res., *112*(E08S13), doi:10.1029/2006JE002845.
Vincendon, M., Y. Langevin, F. Poulet, A. Pommerol, M. Wolff, J.-P.
Bibring, B. Gondet, and D. Jouglet (2009), Yearly and seasonal variations
of low albedo surfaces on Mars in the OMEGA/MEx dataset: Constraints
on aerosols properties and dust deposits, *Icarus*, *200*, 395–405,
doi:10.1016/j.icarus.2008.12.012.
Wanner, W., X. Li, and A. H. Strahler (1995), On the derivation of kernels
for kernel-driven models of bidirectional reflectance, *J. Geophys. Res.*,
100, 21,077–21,090.
Wiseman, S., R. E. Arvidson, M. J. Wolff, R. V. Morris, F. P. Seelos, M. D.
Smith, D. Humm, S. L. Murchie, and J. F. Mustard (2012), Retrieval of
atmospherically corrected CRISM spectra using radiative transfer modeling,
in *Lunar and Planetary Science Conference*, 2146.
Wolff, M. J., M. D. Smith, R. T. Clancy, R. Arvidson, M. Kahre, F. Seelos
IV, S. Murchie, and H. Savijärvi (2009), Wavelength dependence of dust
aerosol single scattering albedo as observed by the Compact Reconnais-
sance Imaging Spectrometer, *J. Geophys. Res.*, *114*(E00D04),
doi:10.1029/2009JE003350.